Design and Evaluation of an Electromagnetic Band Gap Structure for Self-Interference Reduction in mmWave Full-Duplex Systems

by

Adewale Kehinde Oladeinde

A dissertation submitted in partial fulfillment of the
requirements for the degree of

Doctor of Philosophy
in
Electrical and Computer Engineering

Dissertation Committee:
Branimir Pejcinovic (Chair)
Ehsan Aryafar (Co-Chair)
Fu Li
David Burnet

Portland State University
2025

Abstract

Full-duplex (FD) wireless is a new technology that allows a device to transmit and receive at the same time and on the same frequency band. It has the potential to double the capacity and spectral efficiency of a wireless link compared to the family of conventional half-duplex wireless systems. The key challenge in implementing FD wireless communication is self-interference (SI): a node's transmitting signal generates significant interference to its receiver. Several previous studies have demonstrated the potential to reduce SI and develop FD radios; however, these studies are mostly limited to sub-6 GHz systems. Previous and on-going research explored various techniques, including analog self-interference cancellation (SIC), digital self-interference cancellation, passive self-interference cancellation, and combinations of these approaches.

However, at millimeter wave (mmWave) frequencies, the sizes of components decrease significantly in relation to their wavelength, leading to a more compact form factor for mmWave designs. This miniaturization allows for the possibility of innovative FD design approaches; however, it also presents challenges, such as reduced spacing between components. As a result, implementing analog or digital

SIC techniques using robust component devices for mmWave radio and wireless applications demands careful consideration and adaptation.

Furthermore, the transceiver architecture developed for FD solutions at sub-6 GHz frequencies requires modifications to effectively transition to mmWave applications, highlighting the need for architectural advancements in both the digital and analog SIC sections of the transceiver. By addressing these challenges, we can improve the performance and functionality of FD mmWave systems.

This dissertation investigates the potential of a passive solution for SIC at the mmWave frequency of 28 GHz. The research study approach involves the design and integration of a novel electromagnetic band gap (EBG) structure within a substrate design of transmit (Tx) and receive (Rx) antenna arrays. The research investigates novel EBG structures aimed at mitigating planar and surface wave coupling between Tx and Rx antennas within the reactive near-field region of the antenna system. By attenuating these undesired coupling mechanisms, the EBG structure effectively reduces SI to levels that permit reliable reception of the desired signal in a FD operation.

The Tx and Rx antenna system considered for this research comprises unit antenna (single Tx and Rx) elements and Multiple Input Multiple output (MIMO) antenna arrays (1x4 and 4x4). The designs were also fabricated for testing, measurement, and comparison to simulation data. The simulation and manufacturing of prototype antenna and novel EBG designs took into account manufacturing process variations, and substrate material permittivity changes due to temperature and humidity effects.

Furthermore, the design of the unit and MIMO antenna array was validated through passive measurement in an anechoic chamber and using a Vector Network Analyzer (VNA) to determine and compare measured antenna performance metrics with simulated data.

The novelty of our EBG designs lies in the substantial reduction of effective capacitance compared to conventional mushroom-type EBG structures operating at 28 GHz. This reduction is achieved through miniaturization of the unit cell, which allows a greater number of EBG elements to be integrated within a fixed footprint. The miniaturization and effective capacitance change of the novel EBG results in enhanced suppression of surface and leaky wave modes. Consequently, the structure provides wideband isolation between the Tx and Rx antenna arrays, significantly improving FD performance for mmWave applications.

Ultimately, this dissertation aims to advance mmWave FD wireless communication by substantially mitigating SI in the passive RF domain. By addressing SI at the physical layer, the approach has the potential to eliminate reliance on complex and bulky analog cancellation circuits, thereby enabling the development of more compact, energy-efficient, and cost-effective mmWave full-duplex radio architectures.

Dedication

I dedicate this work to my sons, Akolade and Oluwakunmi. I hope my journey inspires you to embrace the valuable lessons of perseverance and hard work: "Cows don't give milk; it has to be extracted drop by drop - Promod Batra".

Acknowledgments

Managing a full-time job, fatherhood, and the pursuit of a doctorate presented considerable challenges. However, with the Grace of the Almighty, I was able to complete my PhD program.

I would like to express my sincere gratitude to my advisor, Prof. Branimir Pejcinovic, for taking a chance on me and agreeing to be my PhD supervisor when I was seeking a PhD program at Portland State University. This opportunity arose when other professors in the faculty were hesitant to add a full-time employee to their research teams due to past experiences with former full-time employees dropping out of PhD programs. He has been an invaluable support throughout my PhD journey, particularly during the design, manufacturing, and measurement stages of my prototype development and also a guide to achieving my required publications towards my Ph.D program. Given the demanding nature of my full-time job and my transitions between employers, his assistance in managing my PhD timeline and making sure that I met all the requirements was invaluable.

I would also like to express my gratitude to my co-advisor Prof. Ehsan Aryafar for taking a chance on me and welcoming me into his research group to explore a pioneering topic in wireless communication. His guidance has been invaluable in shaping my publications and final thesis idea. His support played a crucial role in making my graduate school experience truly rewarding.

My sincere gratitude goes to my advisory committee members, Prof. Fu Li and Prof. David Burnet for agreeing to be part of my committee and for their insightful feedback and advice. Their availability and valuable counsel throughout my Ph.D. studies were crucial.

I wish to also extend my heartfelt gratitude to the department chair, Prof, Martin Siderius, and Graduate Program Director, Prof, Douglas Hall for their unwavering support throughout my Ph.D. journey. Their support were instrumental in making my Ph.D. program possible.

I am immensely grateful for my lovely wife, Titilope and my best friend, whose unwavering support and love have been instrumental in this journey.

My love and appreciation go to my mother, Illegbunem, the pillar of our family. Her strength has laid the groundwork for my achievements, and her influence motivates me to reach my full potential.

I am grateful for the financial support received from both Intel Corporation and Nvidia Corporation for the entire doctorate program.

Table of Contents

Acronyms

FD - Full-Duplex

SI - Self-Interference

SIC - Self-Interference Cancellation

EBG - Electromagnetic Bang Gap

Tx - Transmitter

Rx - Receiver

MIMO - Multiple Input Multiple Output

mmWave - millimeter Wave

VNA - Vector Network Analyzer

AR/VR - Augmented Reality/Virtual Reality

AI - Artificial Intelligence

nLOS - non-Line-of-Sight

PCB - Printed Circuit Board

QoS - Quality of Service

UE - User Equipment

D2D - Device to Device

6G - 6th Generation

BS - Base Station

FDD - Frequency Division Duplex

TDD - Time Division Duplex

HD - Half-Duplex

UL - UpLink

DL - DownLink

IAB - Integrated Access and Backhaul

HIS-nSEBG - High Impedance Surface novel Stacked EBG

IC - integrated Circuits

DGS - Defected Ground Structure

UC EBG - Uniplanar Circular EBG

PEA - Partila Economic Area

WiFi - Wireless Fidelity

ADC - Analog to Digital Converter

RF - Radio Frequency

CMOS - Complementary Metal-Oxide Semiconductor

HFSS - High Frequency Structure Simulator

FSS - Frequency Selective surface

PBG - Photonic Band Gap

TM - Transverse Magnetic

TE - Transverse Electric

OTA - Over-The-Air

GND - Ground reference

AUT- Antenna Under Test

2.92M - 2.92 Male connector

2.92F - 2.92 Female connector

VSWR - Voltage Standing Wave Ratio

PCR - Parallel Coupled line Resonators

CCL - Capacitively Loaded Loop

NFR - Near Field Resonators

SRR - Split Ring Resonators

FDGS - Fractal DGS

ECC - Envelope Correlation Coefficient

List of Tables

List of Figures

Chapter 1

Introduction

The demand for wireless capacity is exploding due to emergent applications, ranging from augmented/virtual reality (AR/VR), artificial intelligence (AI), to massive cellular access [1]–[3]. The spectrum crunch in the legacy sub-6 GHz radio bands has led to the use of higher frequency spectrum, millimeter wave (mmWave) bands, due to the large amounts of spectrum available in these bands. On a parallel front, full-duplex (FD) wireless has recently emerged as a new technology that allows a wireless device to transmit and receive at the same time and on the same frequency band. With FD, the transmitting antenna causes a significant amount of SI on the receiving antenna. Given the co-location of the interfering source compared to the farther desired transmission source, this would completely drown the weaker intended signal in interference, rendering its decoding impossible. Thus, the key challenge in enabling FD so far has been to reduce/eliminate self-interference (SI). Over the past decade, several works have proposed a variety of SI cancellation techniques to enable FD but they are primarily limited to sub-6 GHz systems (e.g., [4], [5], [6] [7] [8]). For example, to enable FD at a small handheld device with 19 dBm transmission power and -95 dBm of noise floor, 114 dB of SI needs to be canceled to enable the receiver correctly interpret and decode the transmitted data. Existing designs use passive cancellation techniques (e.g., antenna design with large separation between transmitter and receiver or transmit and receive antennas with different polarization) and then augment that with active cancellation techniques, which use SI channel information to remove the remaining SI in the analog and/or digital base-band domains. In a FD transceiver such as depicted in Fig. 1.1, signal interference cancellations techniques can be categorized as either active or passive signal interference cancellation. The total SI cancellation requirements are based on implementation methods and can reach up to or more than 100 dB for the maximum realization of FD wireless communication.

From Fig. 1.1, active suppression techniques employ analog and digital cancellation techniques and work based on subtracting the SI signals from the received signal [9]. Published work on active SI cancellation employed different techniques such as using gradient descent [10] technique, an adaptive filtering in the digital domain and focuses on receiver amplifier saturation, dynamic range and attenuation of SI for wide band signals. On the active analog SI cancellation technique, [11] reviews current RF cancellation mechanisms and investigates an efficient mechanism for future wideband systems with minimum complexity while the working principle and implementation details of multi-tap cancelers are introduced, an optical domain-based RF canceler is reviewed, and a novel low-cost design is proposed. Overall, the subtraction process of both active analog and digital self-interference cancellation will be carried out through analogue and digital samples.

The main sources of SI as seen in Fig. 1.1 come from near-field or free space

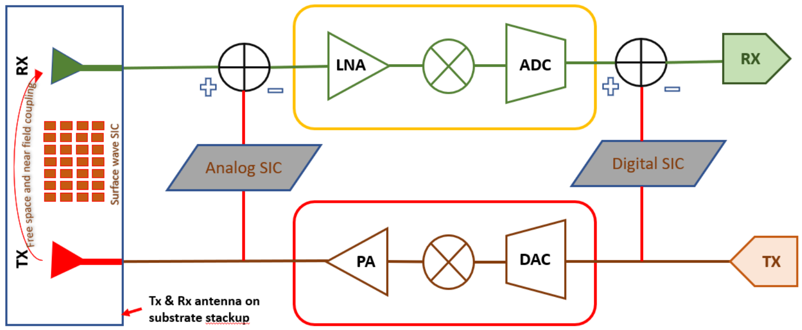

Figure 1.1: FD transceiver link channel showing digital Signal Interference Cancellation (SIC) , analog SIC and passive SIC stages. Tx and Rx antenna with integrated EBG are sharing the same substrate design and common ground plane, thereby increasing the effect of surface wave coupling from Tx to Rx antenna. [9]

coupling and also from an indirect surface-wave coupling between antennas. This is especially evident when two antennas, in close proximity, share the same substrate or the same ground plane. Also, impedance mismatch, transmitter and receiver impairments, non-linearity in the RF front end components and multiple reflections of the emitted signal, i.e., non-Line-of-Sight (nLoS) transmission from the Tx to Rx, contribute to some additional but lower SI level into the receiver. Thus, for an efficient FD transceiver system, the cancellation techniques need to be considered gradually starting from the antenna section to the digital one, passing through the RF/analog part.

More recently, researchers have proposed FD radio designs for mmWave systems. For example, in [12], authors develop a mmWave circulator that connects to the same transmit (Tx) and receive (Rx) antennas and reduces SI. On the other hand, using separate Tx and Rx antennas can provide much more reduction in SI due to over-the-air path loss reduction, which can further simplify the design of active SI cancellation techniques. This can also lead to compact FD designs that can fit in small mobile devices [13] [14] [15].

From Fig. 1.1, the major SI contributions, i.e. the near-field or free space mutual couplings, can be reduced by either increasing the distance between antennas (more than about $\lambda/2$) or by designing Tx antennas radiation pattern to exhibit minimum (or null) in direction toward Rx antenna. Once these antenna-level SI components are strongly reduced, surface waves guided along the interface between the ground plane and the dielectric/air interface, become the most important SI contribution. Suppressing surface-wave coupling between transmit and receive antennas is of prime interest in FD systems. As a result, several mushroom-type EBGs have been studied and their narrow band performance are considered to reduce mutual coupling due to surface waves [16] propagation.

In this research, a new mushroom-type electromagnetic band gap (EBG) structure are introduced and also presented in [17] [18] to reduce surface waves between Tx and Rx antenna in order to improve passive broadband isolation and enable FD wireless communication. Low profile planar unit antenna and multiple input and multiple output (MIMO) (4x4 and 1x4) antenna array are used to demonstrate the effectiveness and electrical characteristics of the proposed EBG in this dissertation. Standard mushroom EBG such as depicted in Fig. 1.2(a) consist of a metallic patches on the top layer which has an effective capacitance used to model electric field between the gap of two metallic patches, while the inductance represents the inductive path of the current flow from one patch to another as seen in Figs. 1.2(b)

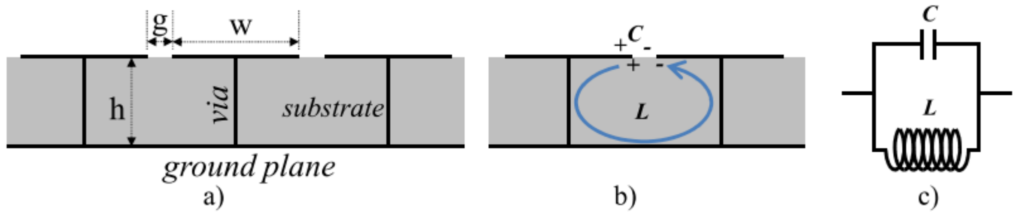

Figure 1.2: Side View of single layer mushroom EBG with square pattern (a); unit cell behavior model (b); and equivalent lumped model (c) [9]

and (c). The inductive loop depends on the substrate or printed circuit board (PCB) thickness and the permeability of the material. In mushroom EBGs, the bandwidth and impedance surface can be estimated using Eqs. 1.1 and 1.2 [9]

$$BW = \frac{\sqrt{(L/C)}}{\sqrt{(\mu_0/\varepsilon_0)}}, \tag{1.1}$$

$$Z = j\frac{\omega L}{(1 - \omega^2 LC)} \tag{1.2}$$

The design and modeling of our EBG employs Eqs. 1.1 and 1.2, where the capacitance of metallic patches were further optimized for smaller form-factor and higher broadband isolation.

1.1 Full-Duplex Communication Applications

FD has been shown to have applications in a variety of scenarios [19], [20] including: base station QoS (Quality of Service) enhancement, femtocells, UEs (User equipment) and D2D (Device to Device) communication, and more recently in

6G (Sixth Generation) mobile communication systems. In this section, we discuss these applications in more detail.

1.1.1 FD for Base Station QoS Enhancement

Vial et. al. [21] suggest that intra-cell FD application would enhance transmitted and received signals by making sure that fading characteristics of both up-link and down-link signal are same. Therefore, making it easier for the Base Station (BS) to correct the received signal. This is unlike BS based on HD (Half-Duplex) using FDD (Frequency Division Duplex) mode, where up-link (UL) and down-link (DL) signal are propagated in different wireless environments, which has higher latency and gets affected by propagation loss and multi-path.

1.1.2 FD for Femtocells

Femtocells are designed to improve spectral and energy efficiency, while offloading traffic from macrocells [22]. In a typical femtocell, which is about 40 m wide in a typical isolated environment [19], users transmit at a much less power than macrocell BSs, which have approximately 1 km range [21]. Reducing transmit power is a direct way to reduce FD signal interference [22]. Therefore, FD is likely to have major applications in femtocell networks.

1.1.3 FD for UE and D2D Communication

Vial et. al. [21] also suggests that when UEs are in close proximity, a D2D communication link is formed without a third party being involved, which offloads traffic from macrocell BS. In traditional half-duplex systems, D2D communication would need to switch between transmit and receive modes, resulting in periods of inactivity and under-utilization of the available spectrum. With FD, both devices can communicate at the same time, doubling the effective capacity of the communication link without needing additional spectrum. This helps overcome the challenge of limited bandwidth in crowded wireless environments.

Also, for D2D communication, the amount of time to send and receive beacons in order to discover peer devices is reduced in FD [23]. Unlike FD, HD discovery time is longer since the equipment cannot receive while it is transmitting.

1.1.4 FD for 6G Applications

FD has been considered as part of technologies that enable 6G wireless technology. One of the main areas where FD is considered prominent is in the integrated access and backhaul (IAB) [24]. The benefit of applying FD to backhaul is significant because it avoids throughput degradation and reduces the communication latency. Also, interference between the access link and backhaul link can be suppressed using passive cancellation through antenna directivity.

1.2 Summary of Dissertation Contributions

Key research contributions for this research include the following:

1. A VicCross EBG design concept was developed, modeled, and simulated to passively suppress SI at mmWave frequencies for full-duplex wireless applications.

2. A new High-Impedance Surface stacked EBG (HIS-nSEBG) design concept was developed, modeled, and simulated for passive signal interference suppression at mmWave frequencies in full-duplex wireless applications. We considered the following two designs:
   (a) single Tx and Rx antenna in a FD system and
   (b) MIMO (1x4) Tx and Rx antenna array in a FD system

1.3 Dissertation Overview

This dissertation focuses on passive self-interference cancellation technique for FD application by proposing a new electromagnetic band gap structure integrated in a substrate or PCB design between transmitting and receiving antennas.

This dissertation is composed of integrating series of conference and journal articles published during the course of the research. The structure of the dissertation is outlined as follows:

1. Chapter 2 discusses the related work on passive SIC for full-duplex wireless at sub-6 GHz and mmWave frequencies.
2. Chapter 3 presents the design of a novel EBG structure for mmWave FD. The extensive simulation and optimization of the novel EBG is described. In addition, a 4x4 cascaded array MIMO antenna is simulated and optimized to carry out the FD Isolation characteristics of the novel EBG. This chapter focuses primarily on a conference paper that addresses in detail the novelty of the new EBG design and its comparison with existing passive isolation devices and components such as mushroom EBG. Importantly, this novel

EBG did not affect the antenna characteristics and metrics necessary for a functional antenna array at mmWave.

3. Chapter 4 presents a stacked nature of the novel EBG design in a unit antenna Tx and Rx FD environment. Based on further simulation analysis of the novel VicCross EBG necessitated by manufacturing requirements and available laminate material, the novel EBG described in Chapter 2 provided higher isolation or mutual coupling reduction in a stack nature where two novel EBGs are constructed on top of each other in a PCB laminate. This chapter focuses on a Journal article publication that presented simulated and lab-measured data for isolation improvement using the novel EBG.

4. Chapter 5 is an extension of the work described in Chapter 4. The stacked novel EBG described is used in a MIMO antenna array environment. The use of MIMO in the characterization of the novel EBG comes with the assumption that most mmWave antennas used in FD application would require higher gain, and as such, antenna array is required. Lab-measured data is presented to quantify the mutual coupling suppression or isolation of antenna arrays working in FD mode.

5. Chapter 6 summarizes the research with a comprehensive discussion and conclusion.

6. Chapter 7 highlights the major contributions of this work towards FD technology in the area of passive self-interference cancellation.

7. Chapter 8 summarizes the limitations of this research and proposes ideas for future work. The limitation described focuses on the active measurement

test bench setup and the inability to incorporate the prototyped antenna array in the test bench system.

Chapter 2

Related Work

This chapter describes some of the related work on FD wireless focusing on passive signal-interference cancellation using EBG structures. For a more comprehensive discussion of the related work, please refer to [8].

If a small handheld device or a femto cell with 20 dBm transmission power and noise floor around -93 dBm is considered. To enable FD, one would need to cancel 20+93=113 dB of SI. This large amount of SI can be removed over multiple stages, namely antenna, analog, and digital cancellation. Fig. 2.1 depicts how different SI cancellation blocks can be incorporated in the design of a FD radio.

Antenna cancellation is primarily a passive SI cancellation technique that arranges Tx and Rx antennas or uses RF elements such as reflectors and absorbers to reduce SI [5], [25]–[30]. *Analog cancellation* is an active cancellation technique that requires knowledge of the SI channel to create a copy of the SI signal in the RF domain and cancel it before the signal is digitized [6], [31]. *Digital Cancellation* is another active cancellation technique that requires knowledge of the SI channel to recreate digital samples of the transmitted signal in the digital domain and subtract them from received samples to remove remaining SI that cannot be removed through antenna and analog cancellation [6].

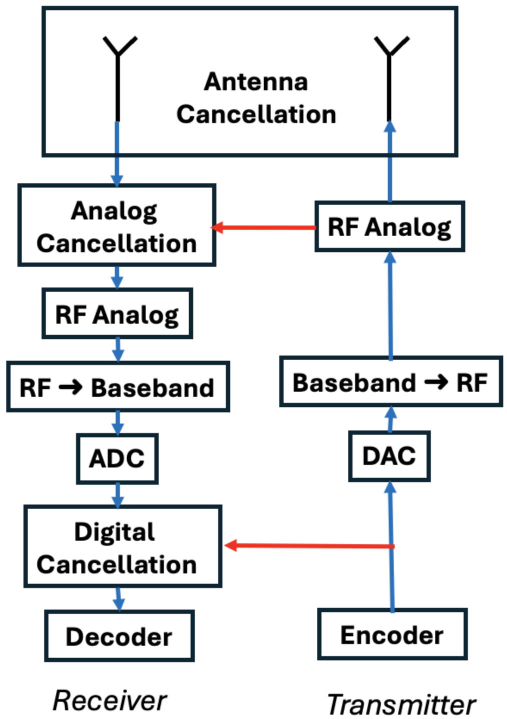

Figure 2.1: In a FD radio, SI is canceled over multiple stages, including antenna, analog, and digital cancellation. Antenna cancellation refers to a plurality of techniques including use of RF absorbers, reflectors, or even additional antennas to reduce SI in the antenna domain.

Majority of the related work in FD radio design are specific to sub-6 GHz radios, with mmWave FD only recently gaining popularity. For example, in [32] authors develop mmWave circulator to reduce SI.

In mmWave systems antenna sizes are very small because their size scales proportionally to the operating wavelength, and thus one can use separate Tx and Rx antennas for even higher reduction in SI due to over-the-air path loss. Other researchers have built a custom integrated circuits (IC) that achieves high bandwidth analog cancellation at mmWave frequencies [33]. Our work can be integrated with this design for further reduction in SI. Another common strategy to reducing coupling energy and interference between Transmitter antenna to Receiver antenna is by increasing separation distance which results in high path loss [34] [35]. The drawback of this technique is that it uses up a larger real estate in designs that requires compact systems. The use of frequency selective surface (FSS) structures have also been deployed to reduce coupling resulting from surface current propagation from antenna to antenna coupling [36]. A 16 dB isolation level was achieved by [37] with a diamond shaped decoupling network with two inverted-F antennas acting as a MIMO antenna. Furthermore, other researchers have explored the use of cross-polarization between a transmitting and receiving antenna elements. In [38] and [39], it was demonstrated that up to 10 dB of isolation can be achieved with cross polarization which effectively attenuates the intensity of coupling waves received by the receiving antenna element. [40] introduced a novel decoupling structure that employed parasitic element to emit orthogonal polarized fields that effectively nullifies the coupling field around a Rx antenna in a collinear FD dipole array, bringing the total isolation to 50 dB. Furthermore, defected ground structure (DGS) [41], and EBG structures [42] and [43] have demonstrated impressive effectiveness in mutual coupling reduction when combined with antenna separation and cross-polarization to over 40 dB of isolation. However, the practical application of using defected groung surface (DGS) and EBG techniques is confined to system with limited number of antenna elements and usually surfer from space constraints especially when large array of antenna element is required to achieve certain gain at mmWave applications. Also, incorporating these additional structures in a system causes complexity and affect the radiation pattern and performance of the antenna array. In [44], authors explored a compact EBG design at 60 GHz and showed that the size of proposed EBG unit cell structure is 78% less than conventional uniplanar EBG and 72% less than uniplanar-compact (UC) EBG operating at same frequency band. It is also claimed that the proposed EBG has 12% more size reduction than any other planar EBG structures at microwave frequencies. On the other hand, [45] used a combination of EBG and choke structure to improve the transmit and receive isolation of X-band large antenna arrays by 30 dB within a 3% bandwidth in the radar operation band. It is important to note that the increased isolation and its associated bandwidth resulted from a combination of using thicker substrate material and combination of choke structures.

In order to mitigate the complexity of design and still maintain the compact design requirement for FD application at mmWave, the proposed unit element HIS-novel stacked EBG is designed to achieve a compact size through the use of stacked slotted patches which has similar planar size structure as EBG designs for much higher frequency (above 30 GHz) applications and is still able to achieve better mutual coupling isolation. The resulting compact nature of the novel EBG is necessitated to alleviate the space constraints in transceiver system designs at mmWave and most importantly reduce the complexity of integration of these EBG components in system design so as not to affect the overall performance of the antenna system.

Table 2.1 summarizes comparison between recent EBG design research for Tx and Rx for both mutual coupling reduction/isolation and for FD application at sub-6 GHz, mmWave frequencies and beyond. The table also shows EBG unit cell size. Note that the operating frequencies and corresponding wavelengths vary which makes direct comparison between sizes difficult.

Table 2.1: Summary of Isolation, EBG/DGS Types and unit cell size

Ref	Operating Frequency	EBG/DGS Type	Unit cell size [length × width]	Total Mutual coupling Level reduction @ 200 MHz BW Isolation of Operating Frequency
[43]	Sub-6 GHz	UC-EBG	$6.6mm \times 6.6mm$	within -30 dB
[46]	2.4 GHz	Fractal Defected Ground Structure	$22.2mm \times 22.2mm$	-60 dB
[47]	12 GHz	Fractal Defected Ground Structure	$8.5mm \times 8.5mm$	-33 dB
[45]	12 GHz	Mushroom EBG with Choke Structures	$1.6mm \times 1.6mm$	-55 dB
[48]	28 GHz	novel EBG & DGS	$2.05mm \times 2.05mm$	-14 dB with EBG -48 dB with EBG & DGS
[49]	28 GHz	Stacked EBG (Our prior work)	$0.6mm \times 0.6mm$	-60 dB and > -80 dB of Peak Mutual coupling reduction
[50]	28 GHz	VicCross EBG (Our work, Ch 3)	$1.3mm \times 1.3mm$	-60 dB and > -68 dB of Peak Mutual coupling reduction
[18]	28 GHz	HIS-nSEBG (Our work, Ch 4)	$1.2mm \times 1.2mm$	-60 dB, -72 dB of peak mutual coupling reduction and -25 dB of Isolation improvement with HIS-nSEBG
[44]	60 GHz	UC-EBG	$0.98mm \times 0.23mm$	< -30 dB
[51]	60 GHz	UC-EBG	$1.1mm \times 1.1mm$	within -20 dB for E-plane coupling and -30 dB for H-plane coupling

Chapter 3

Novel EBG-Based Self-Interference Cancellation to Enable mmWave Full-Duplex Wireless

In this chapter, we introduce the design of a new EBG structure to explore its potential for reducing self-interference in mmWave transceiver antenna designs for full-duplex scenarios. Specifically, we present the "VicCross" EBG, which is integrated into the antenna substrate, and evaluate its performance through simulations in terms of SI reduction, antenna gain, and operating bandwidth. We provide an overview of FD at mmWave and discuss the factors driving its transition from sub-6 GHz to mmWave. We introduce the mmWave MIMO antenna array considered for the transceiver system in FD mode in Section 3.2. We further detaile the antenna array configuration and EBG integration within the antenna array system to characterize and evaluate the novel EBG design for FD wireless in Section 3.3. We finally present the results of our extensive simulations in Section 3.4. The key contributions in this chapter are as follows:

- The main concept of the novel EBG design is to reduce or minimize SI power of the transmitter over a receiver by integrating it between transceiver Tx and Rx antenna arrays. We show that the design effectively reduces the surface wave electric field power between the Tx and Rx arrays. We also derive a circuit model that shows the VicCross EBG with resonant slot on the ground plane creates a high impedance path between the Tx and Rx arrays.

- We conduct extensive simulations using High Frequency Structure Simulator (HFSS [52]) to evaluate performance of mushroom EBG in the mmWave band and further optimize to obtain VicCross EBG. We show that with a combination of bow-tie slot on the ground plane and VicCross EBG between the Tx and Rx antenna arrays, we can achieve up to -70 dB of Tx-Rx isolation at 28 GHz with more than 100 MHz of isolation bandwidth at -60 dB. We also show that VicCross EBG provides up to 20 dB more isolation compared to a conventional mushroom EBG optimized for operation in the 28 GHz band. Finally, we show that VicCross EBG has negligible impact on antenna array performance metrics such as antenna gain, frequency bandwidth, and return loss.

3.1 mmWave Full-Duplex

Millimeter-Wave communication is a promising technology for future broadband wireless networks. While originally designed for semi-stationary applications such as wireless docking and cellular backhaul [53], mmWave communication is nowadays a key component of 5 G and can provide high capacity mobile data rates [54], low latency and ability to support large density of devices on a network.

mmWave systems are typically associated with large bandwidths, e.g., a typical

802.11 ad[1] device routinely uses 2 GHz of bandwidth in the 60 GHz band for communication. However, the amount of mmWave spectrum available to cellular operators depends on the locality and could be far less. For example, even after the recent Federal Communications Commissions (FCC) 5G spectrum auctions [55], AT&T (the second largest mmWave spectrum holder in the US) holds only an average of 630 MHz of mmWave bandwidth [56] in the top 100 PEAs [2]. In addition, AT&T's initial mmWave deployments use only 100 MHz of bandwidth [57]. With mobile data traffic expected to double each year [58], it is therefore imperative to seek solutions that increase the spectral efficiency of mmWave systems.

FD wireless is an emerging solution in this direction, which can double the physical layer spectral efficiency by eliminating SI. With FD, transmission and reception happen on the same time-frequency resource block unlike existing FDD/TDD wireless systems.

FD wireless has been extensively studied over the past decade but majority of the research is dedicated to sub-6 GHz frequency bands [59], [60]. To enable FD, a large amount of SI needs to be canceled. For example, to build a FD wireless fidelity (WiFi) radio with 20 dBm transmission power and -90 dBm noise floor, 110 dB of SI needs to be canceled. In another example, if we consider the following example in the context of contemporary femto-cell cellular systems [61] and based on data provided in Table 10-2 in [61], femto base stations and mobile handsets transmit at 21 dBm with a receiver noise floor of -100 dBm. If we assume 15

[1] WiFi mmWave standard **80211ad**.

[2] PEA: Partially Economic Area, which is a unit of area used by FCC in assigning radio licenses **FCCPEA**.

dB isolation between the base station's transmit and receive signal paths, then the base station's self-interference will be 21 $-15-(-100) = 106$ dB above the noise floor. Thus, for a full-duplex base-station to achieve the link SNR equal to that of a half-duplex counterpart, it must suppress self-interference by more than 106 dB, see Fig 3.1.

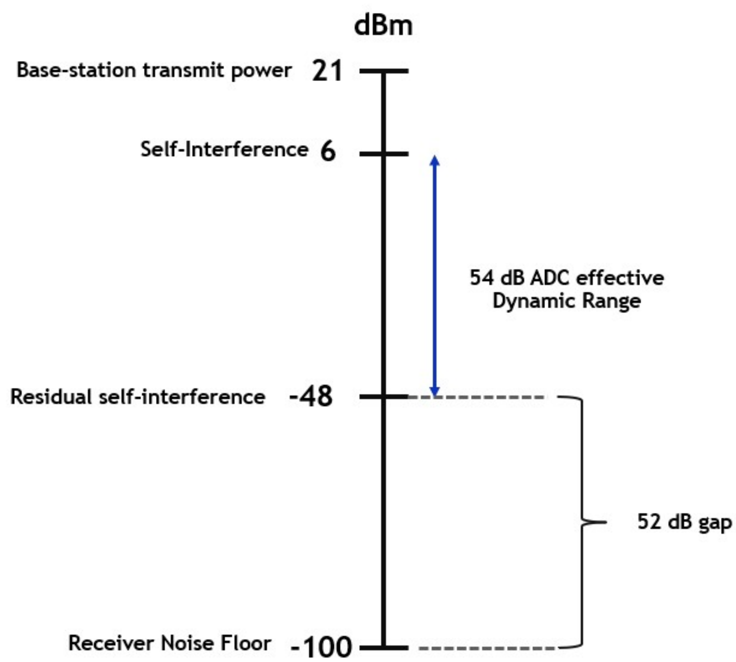

Figure 3.1: Illustrative example of residual self-interference motivated by contemporary femto-cell cellular systems [61]. Even with perfect digital-domain self-interference cancellation, the effects of limited ADC dynamic range cause a residual self-interference floor that is 52 dB above the desired receiver noise floor.

Existing techniques remove the SI at multiple stages, e.g., SI can be initially removed through passive cancellation (e.g., specific antenna design), then possibly with active RF/analog cancellation, and finally through digital cancellation, which removes the remaining SI that cannot be canceled through passive and active RF cancellation in the digital base-band. Scanning the literature on self-interference cancellation, we observe from the literature that different proposed techniques use a combination of wireless-propagation-domain techniques [62] [63] [64], analog-circuit-domain techniques [65] [66] [67] and/or digital-domain techniques [68] [69] [70].

More recently, the community has started to tackle the problem of mmWave FD radio design. CMOS RF cancellation techniques have been proposed in [12], [71], however, these designs are all limited to a small number of antennas (e.g., 1 transmit and 1 receive antenna). Real-world mmWave radios, on the other hand, use an array of antennas to increase the beamforming gain and compensate for the high path loss associated with mmWave frequencies.

3.2 Antenna Design Configurations

A wireless device with separate Tx and Rx antenna arrays is considered for the following reasons: (i) antenna separation reduces SI by up to 40 dB as shown through simulations in Section 3.4,subsection 3.4.3; (ii) circulator based systems are ill-suited at mmWave frequencies due to larger size and inability to scale to multi-antenna systems, and (iii) smaller antenna sizes at mmWave bands allow us to pack more arrays in the same wireless device.

Each Tx/Rx antenna array studied in this section is composed of four 1x4 series fed patch antennas spaced at 0.5λ (where λ denotes the wavelength) as shown in Fig. 3.2. The Tx and Rx antenna arrays are designed and optimized through simulation on the same substrate system with 1.6λ edge-to-edge spacing. The 1.6λ distance is chosen as a compromise between array port to port coupling and size of the system considered for this application[3]. Each antenna array is optimized for maximum array gain using high-frequency structure simulator (HFSS) full-wave electromagnetic simulation tool. Rogers RO3035 substrate material with thickness of 50 μm along with permittivity and loss tangent values of 3.6 and 0.0015 was employed [72]. Two adjacent patch elements in a 1x4 series fed array are connected using 0.1λ electrical length of transmission line. The first three patches are designed using edge feed while the top patch is designed using inset feed. The first two lower patches have the same width of 0.36λ along with lengths of 0.36λ and 0.45λ, respectively. The two top patches are square shaped with width and length of 0.4λ. The length and width of each patch were determined using Eqs. (4.1)-(4.3) [73]:

$$W = \frac{v_0}{2f_r}\sqrt{\frac{2}{\varepsilon_r}} \tag{3.1}$$

$$L = \frac{1}{2f_r\sqrt{\varepsilon_{reff}}\sqrt{\mu_0\varepsilon_0}} - 2\Delta L \tag{3.2}$$

$$\Delta L = 0.412 \times \frac{(\varepsilon_{reff}+0.3)(\frac{W}{h}+0.264)}{(\varepsilon_{reff}-0.258)(\frac{W}{h}+0.8)} \tag{3.3}$$

here, w, L, and ΔL denote the patch width, patch length, and patch length extension, v_0 is the speed of light in free space, ε_r, ε_0, ε_{reff}, μ_0, and h are relative

[3] We considered a portable wireless device application such as a smartphone.

permittivity, permittivity of free space, effective permittivity, permeability, and thickness of the substrate material, and f_r denotes the mmWave resonant (desired) frequency set to 28 GHz[4].

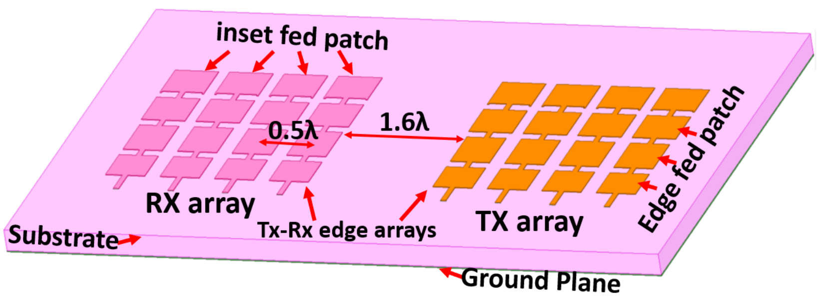

Figure 3.2: 4x4 Tx and Rx antenna arrays on the same substrate material separated by 1.6λ. The location of edge 1x4 Tx-Rx arrays are also specified. The impact of SI is most sever between the two edge arrays due to their proximity.

The input ports to the 4x4 MIMO array for both the transmitter and receiver antenna array are all excited to transmit and receive signals at same time to mimic FD communication. Further, each individual port is designed to be fed with an independent phase shifter to mimic a phased array system. The simulation results of antenna array mutual coupling analysis or transmit and receive signal interference isolation investigated in Section 3.4 use the closest two 1x4 arrays, one from the transmitter and one from the receiver antenna array. These edge arrays are considered to have the worst case mutual coupling characteristics (i.e., have the highest SI). The total coupling coefficient seen by an edge 1x4 array for the transmitter (receiver) array is a summation of the mutual and self coupling

[4]A 5 G software-defined radio was acquired which operates in the 28 GHz band and allows us to experiment with different antenna designs. As part of future work, we plan to compare the results of the simulations presented in this paper with experiments conducted on our 5 G hardware.

coefficients of the 4x4 transmitter (receiver) array.

3.3 Novel EBG Integration with MIMO Antenna Arrays

Electromagnetic band-gap structures are periodic structures that interact and create a stopband to block electromagnetic waves of certain frequency bands by forming a fine, periodic pattern of small metal patches on dielectric substrates. When these structures interact with electromagnetic waves many unique features result. Observables are characteristics such as frequency stop-bands, pass-bands, and band-gaps. However, various terminology has been used to classify these structures depending on the domain of the applications in filter designs, gratings, frequency selective surfaces (FSS), photonic crystals and band-gaps (PBG), etc. EBG refers to such a stop-band as well as to substances (medium to transmit electromagnetic waves) that have such a structure. Broadly speaking, EBG structures are 3-D periodic objects that prevent the propagation of the electromagnetic waves in a specified band of frequency for all angles of arrival and for all polarization states of electromagnetic waves. In practice, however, it is very difficult to obtain such complete band-gap structures and partial band-gaps are achieved. Applications of EBG structures include components of electronic devices to suppress electromagnetic noise as well as design of antenna and other microwave circuits [74]. More recently, a conventional mushroom EBG has been used to reduce SI and enable FD at 3.2 GHz frequency band [75]. In this research, a new EBG design targeted for mmWave frequencies (28 GHz) is developed and its performance is extensively evaluated through simulations.

3.3.1 Mushroom EBG Design and Its Integration with Tx and Rx Antenna Arrays

Mushroom EBG structure is configured from via mediated metal patches as shown in Fig 3.3 arranged periodically on the reference layer.

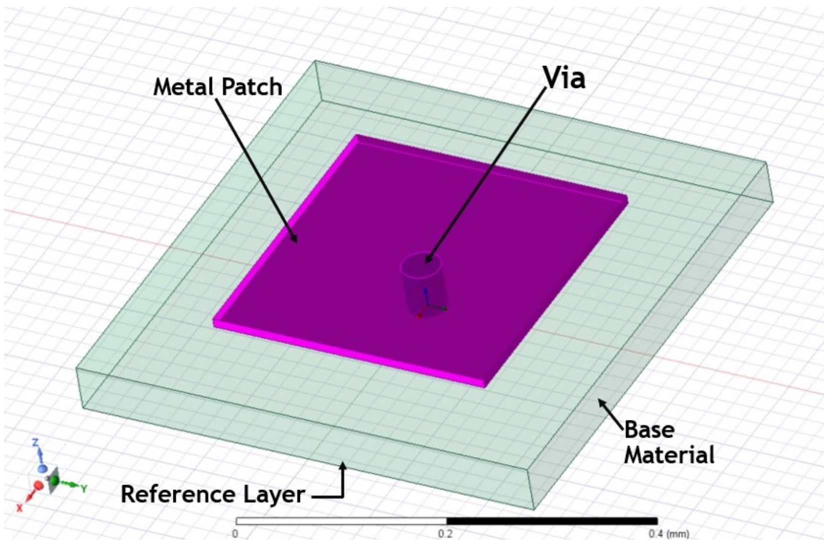

Figure 3.3: A unit cell Mushroom EBG showing metallic patch on a base material with a reference layer. A Plated Through Hole (PTH) Via is located at the center of the patch and is connected to the reference layer on the bottom side.

Mushroom EBG structure configured in this way is known as a composite right/left-handed transmission line and between the right-handed and left-handed frequency bands is the stop-band. In the design of our novel EBG, we start by designing a mushroom EBG composed of metallic square patches with unit element width and spacing between patches of 4 mm and 3.4 mm, respectively. The EBG is designed for a stop band at 28 GHz as shown in Fig. 3.4. The transmission characteristics (S_{12}) of the mushroom-type EBG structure are presented in Fig. 3.4.

The red curve corresponds to the insertion loss when the EBG structure is employed as the reference plane for signal propagation along the trace. In contrast, the blue curve represents the insertion loss of the same transmission line with a continuous solid ground plane serving as the reference plane. The mushroom EBG structure exhibits increased attenuation near the 28 GHz frequency band, indicative of its inherent stop-band behavior, which suppresses signal propagation within this frequency range.

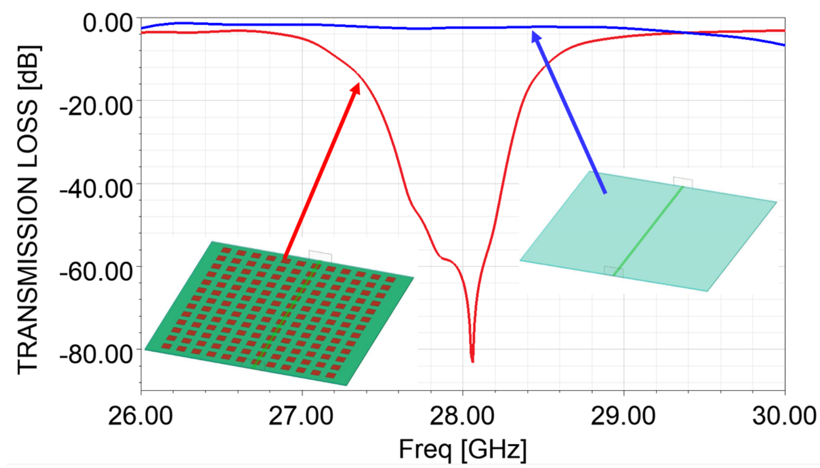

Figure 3.4: Blue curve with close to zero loss shows the transmission loss (S_{12}) of a transmission line using a ground plane as its return path. The red curve shows the transmission loss when mushroom EBG is employed.

Eqs. (3.4)-(3.6) [73] guided our design of the mushroom EBG:

$$C = \frac{W\varepsilon_0(1+\varepsilon_{reff})}{\pi}\cosh^{-1}(\frac{W+g}{g}) \tag{3.4}$$

$$L = 2\times 10^{-7}\times h\times[\ln(\frac{2h}{r})+0.5(\frac{2r}{h})-0.75] \tag{3.5}$$

$$f = \frac{1}{2\pi\sqrt{LC}} \tag{3.6}$$

W is the unit element width, g is the gap between two EBG unit elements, ε_0 and ε_{reff} are free space and relative permittivity of substrate material, h is the substrate material thickness, r is the radius of EBG shorting via, L, C and f are the inductance, capacitance, and resonant frequency of the EBG design.

The initial mushroom design derived from the above theoretical formulas was further optimized in HFSS to provide maximum isolation of up to -80 dB at 28 GHz frequency as depicted in Fig. 3.4.

Fig. 3.5 shows the integrated mushroom EBG with the 4x4 Tx and Rx antenna arrays. The mushroom EBG patch was further optimized to obtain Tx-Rx isolation (SI reduction) of up to -48 dB at 28 GHz as we will show later through simulations in section 3.4.3.

3.3.2 Novel VicCross EBG Integration with Tx/Rx Antenna Arrays

In an attempt to improve the EBG, we started from a mushroom EBG design and its metallic patch was further optimized and modified by cutting slots on the patch to increase inductance and reduce capacitance to form a new EBG design coined “VicCross EBG". We chose the name VicCross due to its shape’s similarity to a Victorian Cross as shown in Fig. 3.6.

The VicCross geometry (Fig. 3.6, top right) consists of a unit cell metal sheet with a two-dimensional lattice of resonant elements (slots), acting as a two dimensional filter to prevent the propagation of electric current. The dimension of

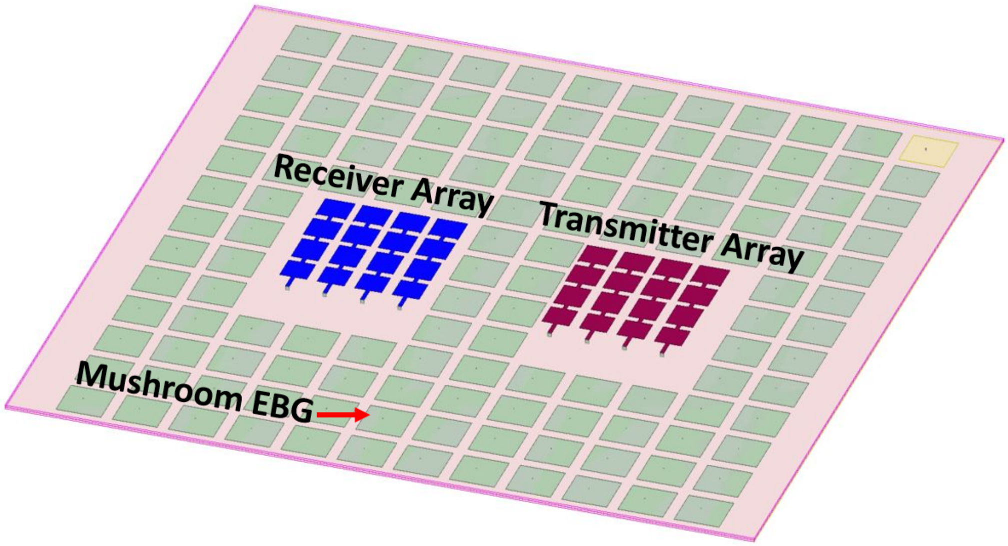

Figure 3.5: Mushroom EBG integrated with 4x4 Tx and Rx antenna arrays. The antenna array elements are enclosed by a mushroom EBG, with sufficient space between the elements and the EBG edge to avoid affecting the efficiency of the antenna array's performance.

the two-dimensional lattice slots are derived through extensive optimization in a bid to further reduce the capacitive characteristics of the EBG patch and thereby increasing its impedance and prohibiting unwanted electric field propagation from one antenna to another. On the other hand, a Defected Ground plane Structure which was used to form a resonant slot, was employed in the ground plane directly under the VicCross EBG to further create a high impedance path to the incident electric field propagation.The DGS shape on the GND plane is termed a "bow-tie" resonant slot.

VicCross EBGs and bow-tie resonant slot on the ground plane (Fig. 3.6, top left) were used between transmit and receiver antenna arrays, while VicCross EBG with shorting via to ground plane were used to surround the antenna arrays (Fig. 3.6, bottom). We will later show in Section 3.4 that the proposed EBG provides up to 20 dB of additional isolation (SI reduction) compared to the conventional mushroom EBG at mmWave 28 GHz Frequency.

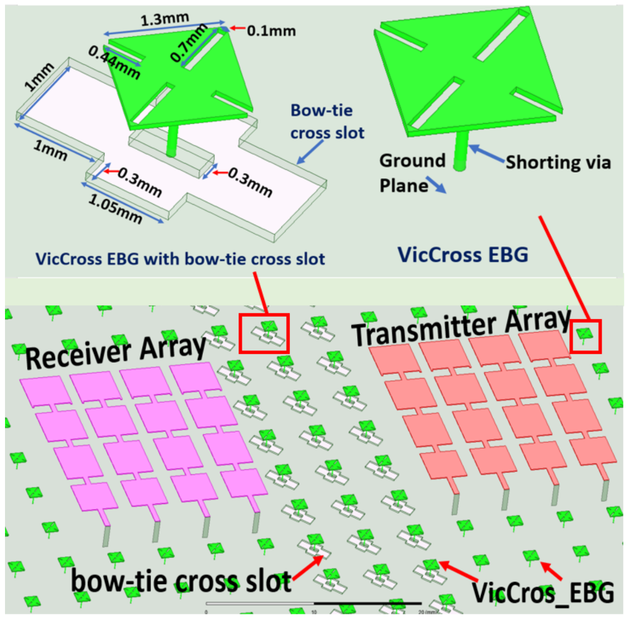

Figure 3.6: 4x4 TX-RX antenna arrays integrated with VicCross EBG. VicCross EBG with bow-tie cross slots are integrated between the Tx and Rx antenna arrays. VicCross EBG also surrounds the two arrays in a periodic manner.

The novel VicCross EBG reduces mutual coupling and is able to isolate transmitted to receiver surface wave currents through the top ground plane and within the substrate. The bow-tie cross slot on the ground plane was designed as a DGS between the transmit and receive array elements in order to increase the inductive path of the electromagnetic wave coupling on the ground plane. Further, VicCross EBG between Tx and Rx array element is designed to have series capacitance to the ground loop inductance in order to further reduce the capacitance of VicCross

EBG patch to the ground plane. A circuit model shown in Fig. 3.7 can be used to describe the lumped element behavior associated with the VicCross EBG and DGS.

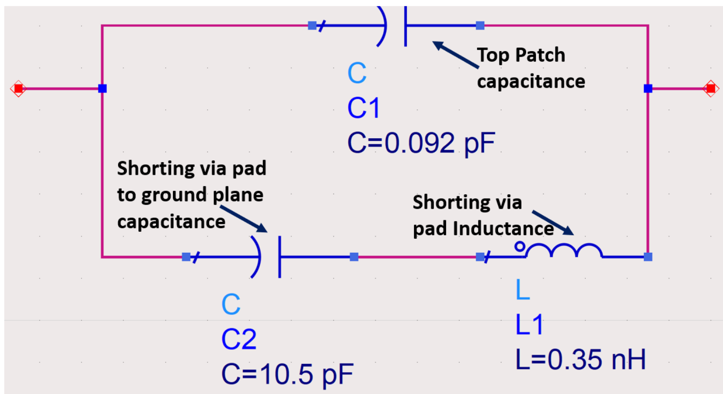

Figure 3.7: VicCross EBG surface impedance circuit model. The component values are reported by the ADS (Advanced Design Suite) software (developed by Keysight), which approximate the VicCross EBG model.

From the equivalent circuit model in Fig. 3.7, at frequencies below the design frequency, the circuit model becomes inductive and supports TM surface waves, whereas at frequencies above the design frequency, the circuit model becomes capacitive and thereby supports TE surface waves. At a narrow band around the LC resonance point (frequency), the impedance between the Tx and Rx antenna arrays becomes very high.

The VicCross EBG is designed so that its surface wave band gap covers our desired antenna resonant frequency bandwidth. Note that, as shown in Fig. 3.6, there is no EBG structure under the antenna arrays. Further, the thickness of the substrate under the antenna arrays is the same as when EBG is not used. This is to keep the antenna frequency bandwidth of our design similar to the design with no

EBG. The edge gap between the antenna array and surrounding VicCross EBGs is carefully chosen through simulation to be a minimum of 0.13λ to not affect the frequency bandwidth and performance characteristics of the antenna array and at same time to effectively reduce the surface wave propagation.

3.4 Performance Evaluation

In this section, we characterize the performance of the VicCross EBG through extensive simulations using HFSS. First, as a baseline for comparison, we consider the antenna design with separate Tx and Rx antenna arrays but with no EBG (i.e., Fig. 3.2). Next, we show that the VicCross EBG has only a minor impact on the antenna performance metrics (frequency bandwidth, gain) but substantially increases the Tx-Rx isolation (i.e., substantially reduces the SI power). Finally, we end our performance evaluation by demonstrating the electric field coupling between the Tx and Rx arrays.

3.4.1 Antenna Frequency Bandwidth.

Fig. 3.8 shows the active S-parameter plot of 4x4 array ports. Active S-parameters [76] represent the reflection coefficients for the various 1x4 array excitations and is an important performance metric for active phased array antennas. Active S-parameter of transmitter and receiver edge ports (i.e., the two closest Tx and Rx 1x4 arrays) were plotted in Fig. 3.8 for both when EBG is not employed (blue curve) and when VicCross EBG with bow-tie ground resonant slot is used (red curve). For each design configuration, the series-fed transmitter (Tx) and receiver (Rx) edge ports demonstrate consistent and comparable impedance matching characteristics. The plots shown in Fig. 3.8 correspond to the return loss (S_{11} or S_{22}) responses, representing the impedance bandwidth of individual series-fed Tx or Rx edge ports. These results validate the symmetry and uniformity of the port performance across the respective configurations. In antenna design, a return loss of -10 dB or lower is typically desirable. From Fig. 3.8, we observe that VicCross EBG has a 1.9 GHz impedance bandwidth, which is about 20 MHz less than the impedance bandwidth when EBG is not employed. This represents roughly 1% change and is considered negligible.

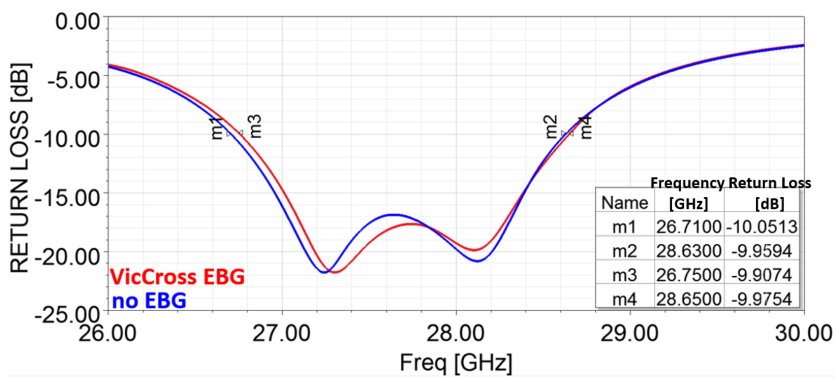

Figure 3.8: Active S-parameter plot showing VicCross EBG and noEBG frequency bandwidth at -10 dB return loss.

3.4.2 Antenna Gain.

Fig. 3.9 demonstrates the Tx (Rx) 4x4 antenna gain in both E and H planes. It is observed that the VicCross EBG slightly increases the gain but narrows the beam-width. We also observe up to 5 dB increase in side lobe level (SLL) and back side lobe which are due to the interaction of the reflected surface waves caused by the

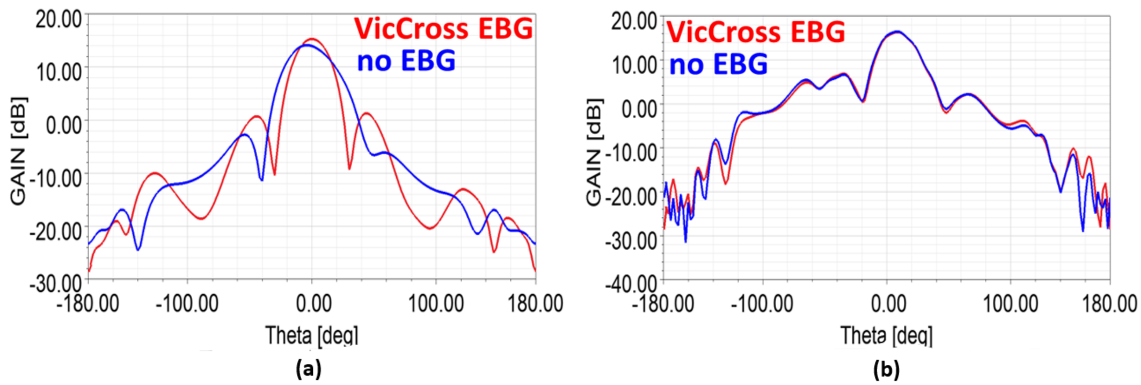

Figure 3.9: (a): E-plane gain. VicCross EBG slightly increases the gain but narrows the beamwidth. We also observe up to 5 dB increase in side lobe level; (b) H-plane performance of the VicCross EBG and no EBG are quite similar.

VicCross EBG, changes in electrical characteristics of the ground plane shape, and the antenna radiation characteristics. We hypothesize that a further optimization of the EBG placement near the antenna array could improve the SLL and back lobe performance. On the other hand, H-plane performance of the VicCross EBG and no EBG are quite similar.

Next, we plot the bore-sight gain variation across the frequency bandwidth in Fig. 3.10. We observe that VicCross EBG and no EBG antenna system exhibit a similar gain vs frequency performance. In both designs, a maximum gain of 18.5 dB is reached at 28 GHz, which remains the same as the frequency increases.

3.4.3 Tx-Rx Isolation (SI reduction)

We next characterize the reduction in SI power for three scenarios: (i) no EBG, (ii) conventional mushroom EBG (discussed in Sub-section 3.3.1), and (iii) VicCross

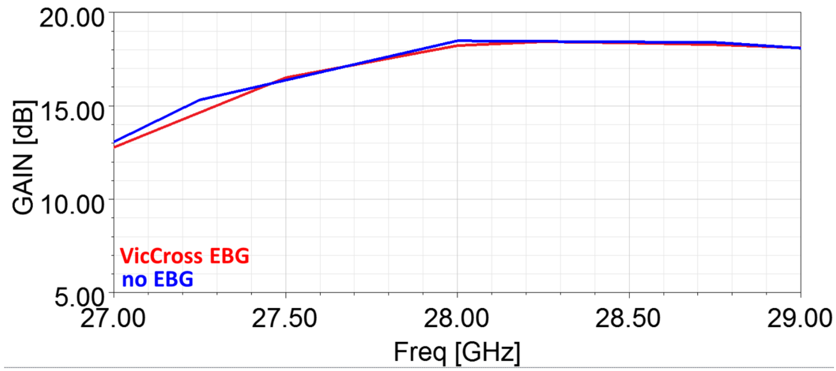

Figure 3.10: Tx/Rx antenna array gain as a function of frequency. VicCross EBG has negligible impact on the antenna gain across the 2 GHz (27 GHz to 29 GHz) frequency bandwidth of simulation.

EBG with bow-tie resonant slot on ground plane. Fig. 3.11 shows the Tx-Rx isolation across the three schemes. We observe that even without the EBG, the Tx-Rx isolation ranges between -35 dB and -40 dB, primarily due to the separation between the Tx and Rx antennas. The Mushroom EBG improves the isolation to -48 dB at 28 GHz, as shown in the same figure, providing an additional 13 dB of isolation compared to the antenna array without the EBG. Additionally, the Mushroom EBG demonstrates consistent performance across different frequencies. Our proposed VicCross EBG with bow-tie cross slot provides up to -70 dB of isolation at the 28 GHz frequency with more than 100 MHz of isolation bandwidth at -60 dB [5]. At its maximum isolation point, this is 32 dB more isolation when compared to the no EBG antenna array and 20 dB more isolation when compared to the antenna array with conventional mushroom EBG. Its important to note that

[5] Wireless applications that use this bandwidth will have Tx and Rx isolation of more than 60 dB. For example, AT&T's initial mmWave deployments use only 100 MHz of bandwidth [57]. Therefore, lower isolation at adjacent frequencies will not impact the performance of the FD communication link.

the port to port isolation plots in Fig. 3.11 correspond to active s-parameter plots of the edge 1x4 Tx and Rx arrays, where the SI power is highest.

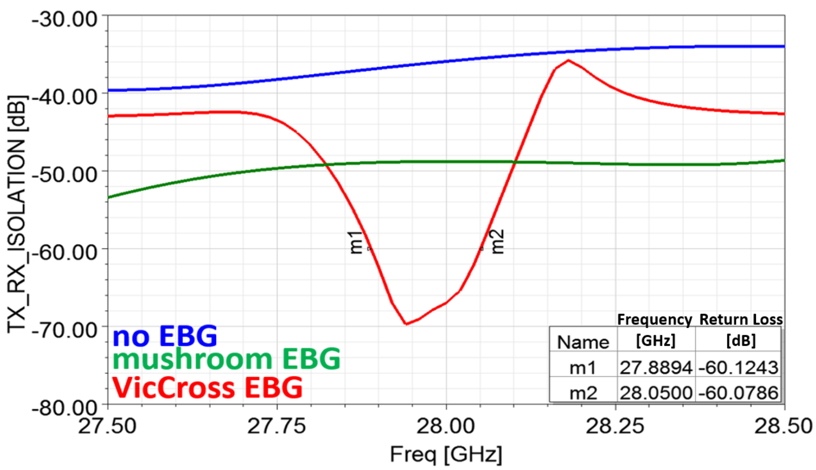

Figure 3.11: Transmitter-Receiver isolation with no EBG (blue), with mushroom EBG (green) and VicCross EBG (red). VicCross EBG with bow-tie cross slot provides up to -70 dB of isolation at 28 GHz frequency with more than 100 MHz of isolation at -60 dB.

3.4.4 Tx-Rx Electric Field Coupling.

We next investigate the electric field coupling between the Tx and Rx antenna arrays resulting from the surface wave radiation through the substrate for antenna system with and without EBG and plot them in Fig. 3.12. Our simulation in Fig. 3.12(a) shows a higher coupling of more than 57 dB(V/m) with no EBG, while Fig. 3.12(b) shows reduction in coupling down to 46 dB(V/m) between the VicCross EBG and the antenna array. The VicCross EBG interaction with the substrate material properties resulted in a high impedance path for the surface wave electric field to propagate from the Tx to Rx array.

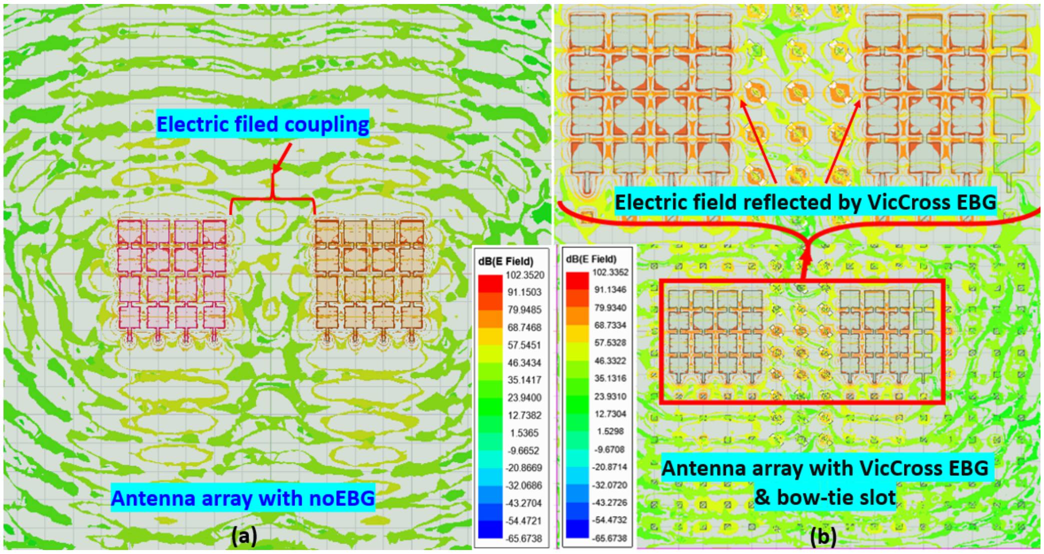

Figure 3.12: (a): no-EBG substrate Electromagnetic field propagation; (b) VicCross EBG substrate Electromagnetic field propagation. VicCross EBG reduces the coupling by up to 46 dB (V/m) between the EBG and antenna array.

In summary, through extensive simulation through HFSS tool, we showed that in a 4x4 MIMO array antenna FD environment, a new novel EBG coined "VicCross" EBG FD environment can achieve up to -70 dB of Tx-Rx isolation at 28 GHz with more than 100 MHz of isolation of bandwidth at -60 dB. The novel VicCross EBG provides up to 20 dB more isolation compared to a conventional mushroom EBG optimized for operation in the 28 GHz band and has negligible impact on antenna performance metrics.

Chapter 4

MmWave High Impedance Surface novel Stacked EBG: Simulation and Characterization

In this chapter, we present the design of a stacked novel EBG structure that creates a high-impedance path for electromagnetic waves traveling between the transmit and receive antenna elements. The EBG configuration consists of stacked novel EBG patches on layers 1 and 2 of a 4-layer stack-up, and it is evaluated through both simulations and laboratory measurements in a unit antenna transmitter and receiver setup. The chapter also covers the design, optimization, prototyping of the unit antenna elements, stacked novel EBGs, and their integration into a mmWave FD System.

To meet specific manufacturing requirements, the novel EBG presented in this chapter is a derivative of the VicCross EBG discussed in Chapter 2. To comply with manufacturing rules and requirements, meet isolation standards equal to or exceeding those of VicCross EBG, and enable the fabrication and characterization of the novel EBG in a stacked configuration, we re-optimized the VicCross EBG using HFSS simulations. Passive measurements and over-the-air (OTA) characterization of the unit antenna elements were performed in an anechoic chamber to compare simulated results with measured data for an antenna design intended to operate at mmWave frequencies for full-duplex applications.

Through extensive evaluations, we demonstrate that: (i) compared to an architecture without EBGs, the proposed novel stacked EBG design achieves an additional 25 dB of isolation over a 1 GHz bandwidth, providing 10 times more isolation bandwidth than the VicCross EBG, (ii) the unit antenna structure offers 1 dB higher main lobe antenna gain and 1 dB lower side lobe levels compared to the no EBG architecture, (iii) the unit antenna element maintains over 1 GHz of bandwidth at -10 dB return loss, and (iv) the unit antenna structure, along with the integrated antenna and stacked EBG system, shows close agreement between simulated and measured performance evaluation results.

The overall goal of this chapter is to evaluate how our new EBG design would work in a real-world environment. To achieve this, we first propose using a single transmit and receive antennas while embedding a High Impedance Surface novel Stacked Electromagnetic Band Gap (HIS-nSEBG) structure in between them to reduce SI. We later introduced an array of transmit and receive antennas of same antenna design while embedding the new EBG to characterize SI. The following outlines the design and evaluation carried out in this chapter

- **Design:** We outline the design process for a unit patch antenna, a stacked novel EBG, and the integration of these stacked novel EBGs between the antennas. The initial design of the VicCross EBG was refined through extensive HFSS simulations to achieve an optimal balance between key performance metrics, including return loss, frequency bandwidth, SI reduction, and antenna gain. Additionally, we present the theoretical modeling of the band gap structure of the stacked novel EBG as an LC circuit and explain how the different components of the EBG contribute to the inductance (L) and capacitance (C) characteristics of the LC circuit.

- **Evaluation:** We conduct comprehensive evaluations of our design through both HFSS simulations and laboratory measurements of a prototype. Additionally, extensive over-the-air measurements are performed in an anechoic chamber. Our results demonstrate a close agreement between simulations and real-world measurements, with only minor deviations due to manufacturing and measurement factors. For instance, we observe an average of 2 dB difference in SI reduction between simulation and measurement. However, larger discrepancies can occur, such as more than 10 dB differences in return loss predictions at lower and higher frequencies, particularly in the frequency bandwidth (return loss) plot. Furthermore, we show that the proposed design, compared to a system without EBGs, achieves over 25 dB of additional SI reduction over a 1 GHz bandwidth, as well as more than 1 dB higher main lobe antenna gain and 1 dB lower side lobe levels.

This chapter is organized as follows. In Section 4.1 We describe the design of a unit element patch antenna and characterize its return loss, antenna gain, and frequency bandwidth through Ansys HFSS [77] simulations and measurements in an anechoic chamber. We discuss the optimization and design of novel HIS-nSEBG and how to integrate them between Tx and Rx patch antennas in Sections 4.3 and 4.4, respectively. We characterize the overall antenna performance including gain and port-to-port isolation (i.e., SI reduction) in Section 4.5.

4.1 Unit Antenna Element Design and Characterization

This section discusses the design and performance evaluation of the unit antenna element designed to characterize the performance of proposed HIS-nSEBG. The unit antenna element is composed of a rectangular patch. Using this antenna element, a Transmit and Receive patch antennas on a single wireless device (substrate or PCB) with an embedded HIS-nSEBG structure in between the two antennas to further reduce SI is described in Section 4.4. The choice for Tx-Rx antennas separation as described in this design are due to the following reasons: (i) antenna separation itself provides more than 30 dB reduction in SI as we show through lab measured data in Section 4.5 and (ii) smaller wavelengths associated with mmWave bands allows us to pack many antennas on the same wireless device.

4.1.1 Design of the Rectangular Patch antenna

An edge-fed rectangular patch antenna is considered for this work to characterize the performance of the proposed HIS-nSEBG because of its ease of fabrication in mmWave bands, ease of integration into circuits and systems, and its simple feed line technique. This is an advantage that comes at the cost of lower antenna gains, narrower bandwidth, and excitation of surface waves. Our design is focused on 28 GHz frequency band, which is used for 5 G cellular mmWave communication.

Fig. 4.1 (top right) shows the 3D view of the rectangular patch antenna implementation on a 4-layer stack-up structure. The top layer of stack-up is used

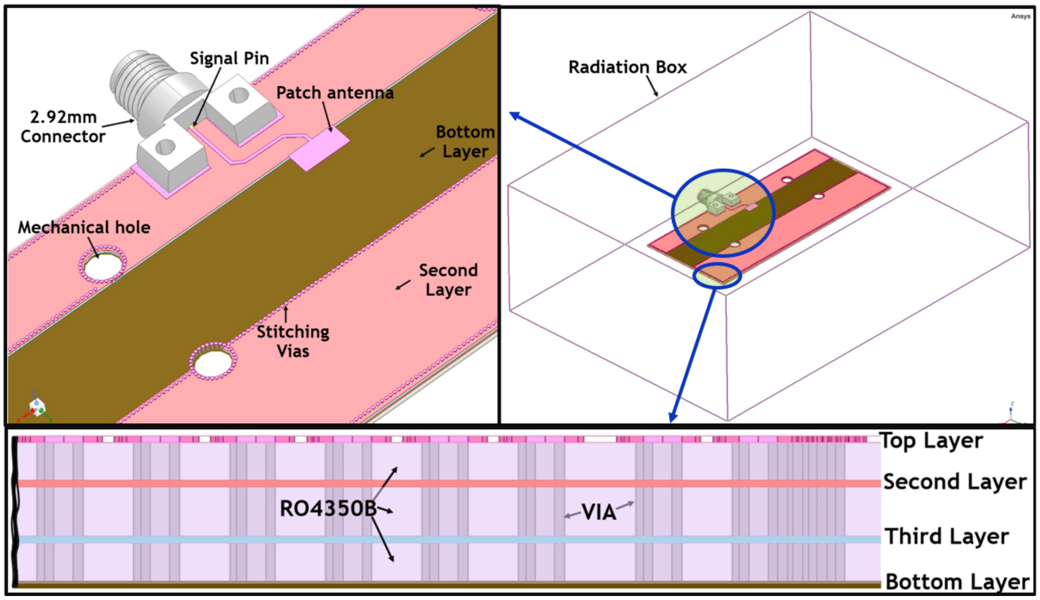

Figure 4.1: Top Left: 3D Model of a unit antenna showing zoomed-in unit Antenna with mechanical holes and connector. Top Right: Unit antenna in radiation box. Bottom: Stack-up with material property and layers.

for a rectangular patch antenna implementation and pad contact for 2.92 mm RF connector connection as shown in Fig. 4.1 (top left). The second layer (L2) is used as ground (GND) reference plane for patch antenna lead-in trace. A rectangular void structure on L2 is created under the patch antenna for improved antenna efficiency. Similar rectangular void structure is created on third layer (L3) to further improve the antenna performance. A solid GND layer is defined at the bottom layer as GND reference, which also has mechanical connection for RF connector assembly. Four Mechanical holes are added to the PCB design to allow for mechanical support of the Antenna Under Test (AUT) during 3D radiation pattern measurements as we will discuss later in Section 4.2. Rogers RT-Duroid laminate RO4350B and RO4450F pre-preg[1] materials with permittivity (Er) of 3.66 and loss tangent (*tand*) of 0.0037 are used for the stack-up construction as depicted in Fig. 4.1 (bottom). The laminate utilizes both 1080 and 1674 glass weave type for controlled impedance and lower resin contents. Inner and outer copper layers are chosen as 1 oz/ft^2 (0.035 mm thickness) with core and pre-preg thicknesses of 0.254 mm and 0.02 mm, respectively, which leads to a stackup thickness of 0.85 mm, an optimal thickness required for the chosen 2.92 mm RF connector assembly.

The overall dimension (Length, Width and thickness) of AUT PCB design, i,e., Length x Width x thickness is 100 mm x 45 mm x 0.85 mm to allow for radiation pattern measurements in an anechoic chamber. The RF connector used in the design is a 50 Ω end launch female 2.92 mm connector with maximum operating frequency of 40 GHz. A 15 mm microstrip transmission line is used to feed the antenna.

In the design of the patch antenna, the length and width were determined using Eqs. (4.1)-(4.3) [78]:

$$W = \frac{v_0}{2f_r}\sqrt{\frac{2}{\varepsilon_r + 1}} \tag{4.1}$$

$$L = \frac{1}{2f_r\sqrt{\varepsilon_{reff}}\sqrt{\mu_0\varepsilon_0}} - 2\Delta L \tag{4.2}$$

[1]Pre-preg is a composite material made from “pre-impregnated” fibers and a partially cured polymer matrix, such as epoxy or phenolic resin, or even thermoplastic mixed with liquid rubbers or resins **prepreg**.

$$\Delta L = 0.412 \times \frac{(\varepsilon_{reff} + 0.3)(\frac{W}{h} + 0.264)}{(\varepsilon_{reff} - 0.258)(\frac{W}{h} + 0.8)} \tag{4.3}$$

Here, W, L, and ΔL denote the patch width, patch length, and patch length extension. v_0 is the speed of light in free space. ε_r, ε_0, ε_{reff}, μ_0, and h are relative permittivity, permittivity of free space, effective permittivity, permeability, and thickness of the substrate material, and f_r denotes the resonant (desired) frequency. The resonant frequency considered for this design is 28 GHz.

4.2 Unit Antenna Characterization

We next proceed to the characterization and the performance evaluation of the fabricated unit antenna element in terms of frequency bandwidth, radiation pattern, and antenna gain. In addition to lab-based measurement data, HFSS [77] based simulation data is also presented to compare with lab measured data. Fig. 4.2 shows a lab setup for the unit antenna performance characterization using a two port Anritsu [79] Vector Network Analyzer. A 2.4 mm cable is connected to the antenna under test via a 2.92 M (Male) to 2.4 F (Female) adapter. VNA calibration was done to shift reference measurement plane to the RF cable connector end point including the adapter. The calibration was done to allow electrical characteristics of the AUT along with its RF connector to be captured without artifact or parasitic from the measured environment and correctly do comparisons with data obtained through simulations.

Fig. 4.3 shows measured and simulated plots for the unit antenna bandwidth

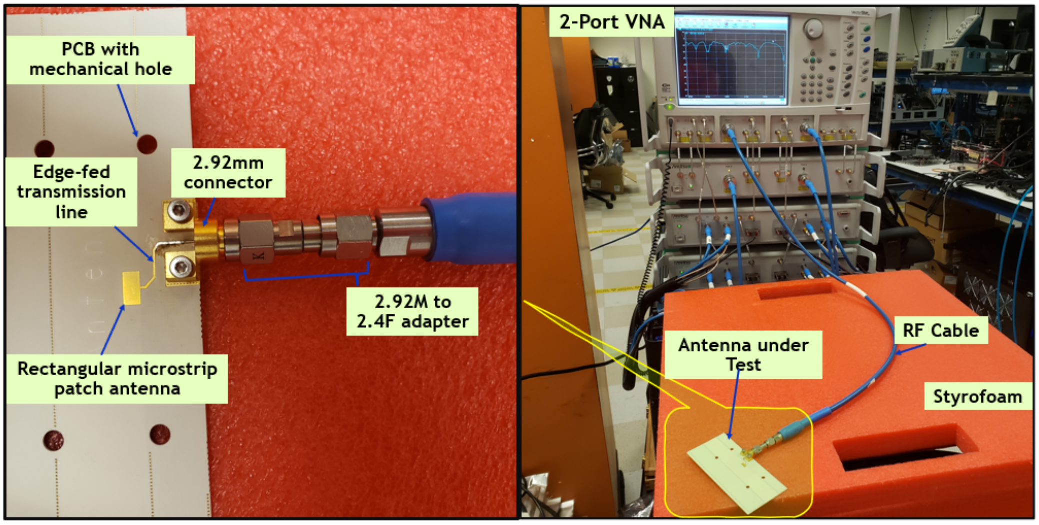

Figure 4.2: Frequency bandwidth and return loss measurement setups for the AUT. Left: Unit antenna on Printed Circuit Board (PCB) and its connector. The connector is attached to a 2.92 mm RF adapter, which is then connected to the VNA through a blue RF cable. Right: Unit antenna lab measurement setup. The Anritsu 2-port VNA is connected to the AUT via a blue RF cable.

performance with good return loss profile agreement across the frequency range. At a desirable return loss of -10 dB or lower [78], measured bandwidth for the unit antenna is 1.2 GHz (27.6 GHz - 28.8 GHz), resulting in a fractional bandwidth of 4.3% and is considered to meet the Gbps data speed for mmWave communication of intended 28 GHz mmWave application. We also observe that simulation results have good agreement with the measurements results, however, the gaps can sometimes be large (more than 10 dB) at lower and higher frequencies.

Fig. 4.4 shows the voltage standing wave ratio (VSWR) of the antenna. At the desired 28 GHz frequency, the VSWR value is 1.06:1. This indicates a higher transmitted power, which also translates to a higher efficiency antenna.

Radiation pattern measurements using an anechoic chamber were also carried

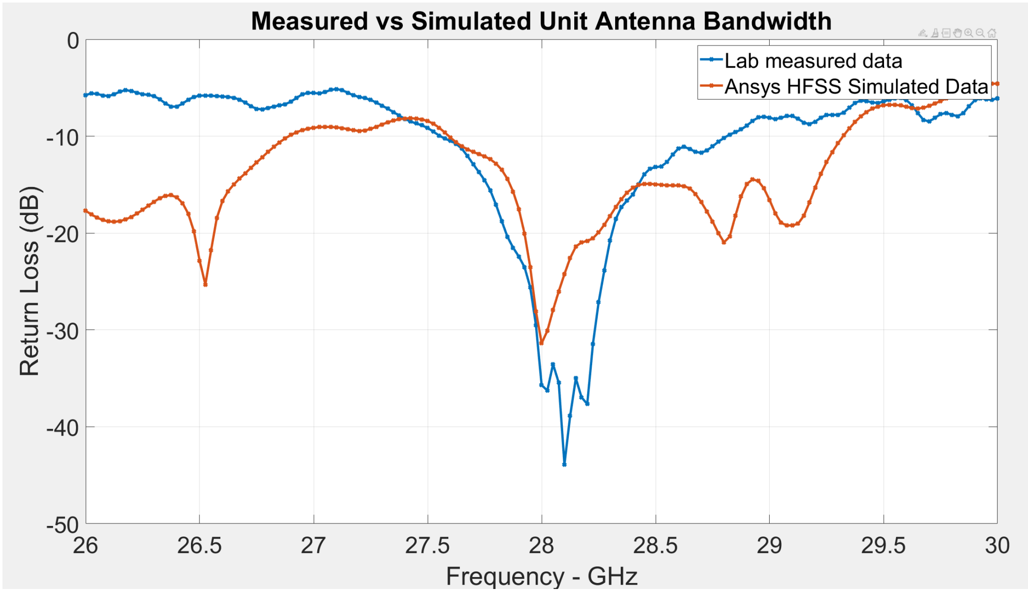

Figure 4.3: S-parameter plots ($|S_{11}|$) showing simulated (red) and measured return loss data (blue). The simulated and measured -10 dB bandwidth is ∼1.8 GHz and ∼1.2 GHz respectively

out to determine the measured 3D electric field radiation of the patch AUT and this was compared against HFSS simulations. Fig. 4.5 shows the Millibox [80] mmWave anechoic chamber used for antenna 3D radiation pattern characterization and measurements, with the designed AUT mounted on a robotic arm on the right side of the chamber. A reference transmitting horn antenna held by another robotic arm on the left side of the chamber is in line-of-sight to the AUT. The distance between the transmitting antenna and AUT is within the far-field distance, which allows for appropriate characterization of the far-field radiation pattern of the AUT. 3D radiation pattern measurements were taken from 26 GHz to 30 GHz frequency band, and by rotating the transmitting antenna both vertically (from -90° to 90°) and horizontally (from -90° to 90°) with a step size of 2°.

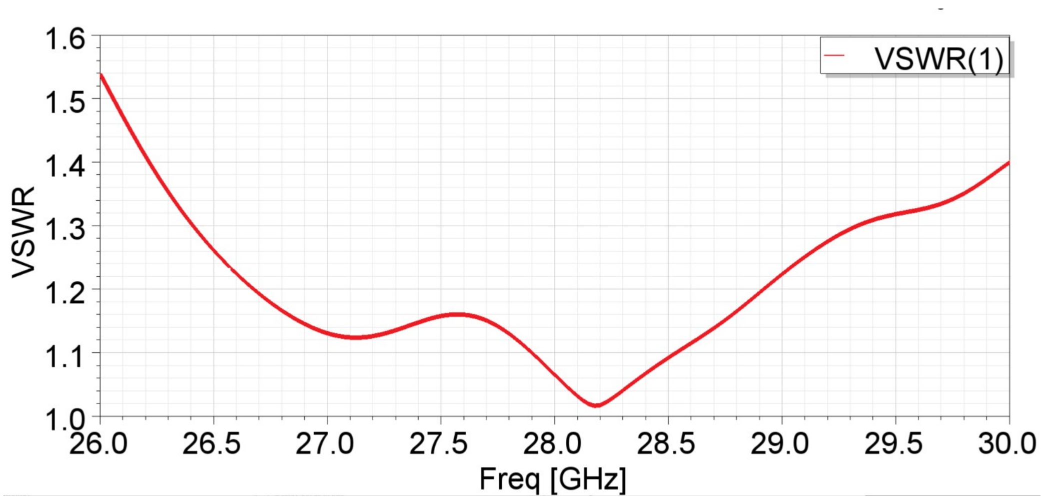

Figure 4.4: Simulated Voltage Standing Wave Ratio (VSWR) of unit antenna element showing 1.06:1 within 28 GHz frequency of interest.

The simulated and measured[2] radiation 3D pattern results for the AUT are shown in Fig. 4.6 with a close agreement between the two radiated field plots. It is observed that the radiated 3D fields plots for both measured and simulated AUT shows maximum radiated gain and nulls in similar phi and theta angle of measurement and simulated plots. The presence of nulls in the measured data which was also observed in simulation is characterized by the the destructive interference of near-filed coupling between the patch antenna element lead-in trace and the connector. However, the performance characteristics of the antenna still met FD mmWave application, as intended Further work of having an array (1x4 for both Tx and Rx) of similar patch antennas with a pitch of $\lambda/4$ and being able to have the connectors placed side-by-side necessitates the current placement architecture of the AUT and its connection with the lead-in trace element. This

[2]Millibox RF engineers assisted in carrying out the radiation pattern measurement

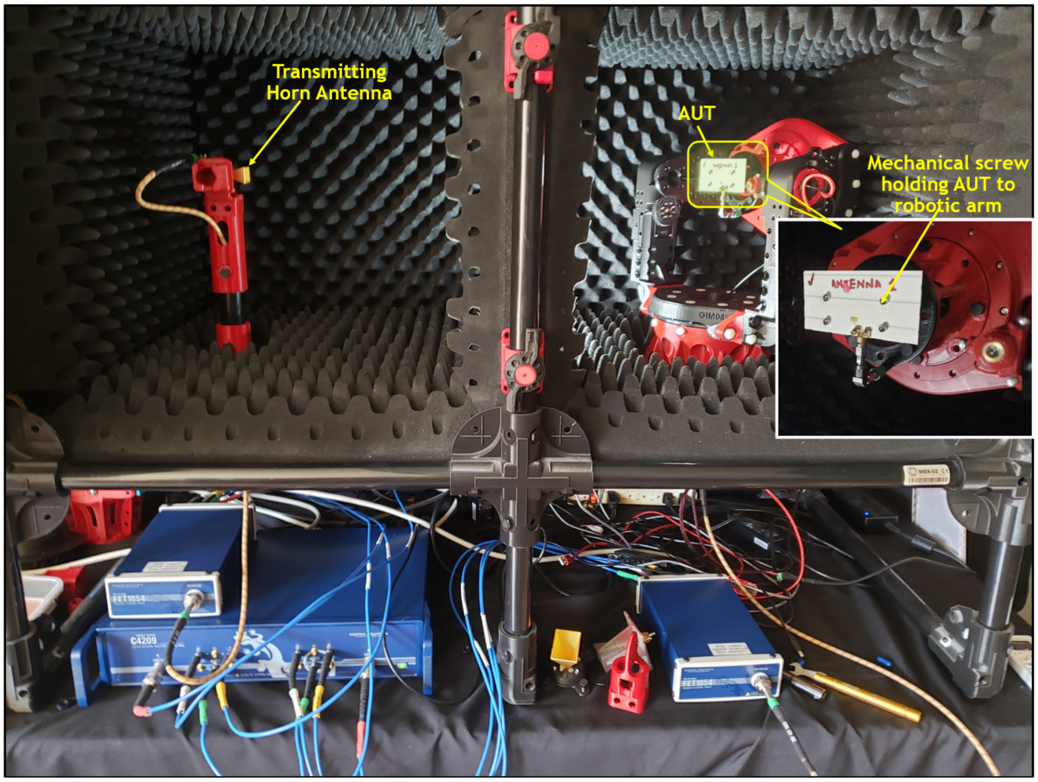

Figure 4.5: Millibox anechoic chamber far-field measurement setup. Left: robotic arm holding a reference horn antenna and Right: Robotic arm holding the antenna under test (AUT) to determine the 3D radiation pattern.

work is described in detail in Chapter 5.

The measured and simulated bore-sight antenna gain variation as a function of frequency is seen in Fig. 4.7. A close agreement is observed between the two plots with only a few dB of difference between measured and simulated results. The proposed antenna design achieved a measured gain of about 4 dBi over 28 GHz and 28.5 GHz frequency range of interest. This is good gain performance for a low profile patch antenna required to be deployed for an array of antenna meant for mmWave full-duplex application.

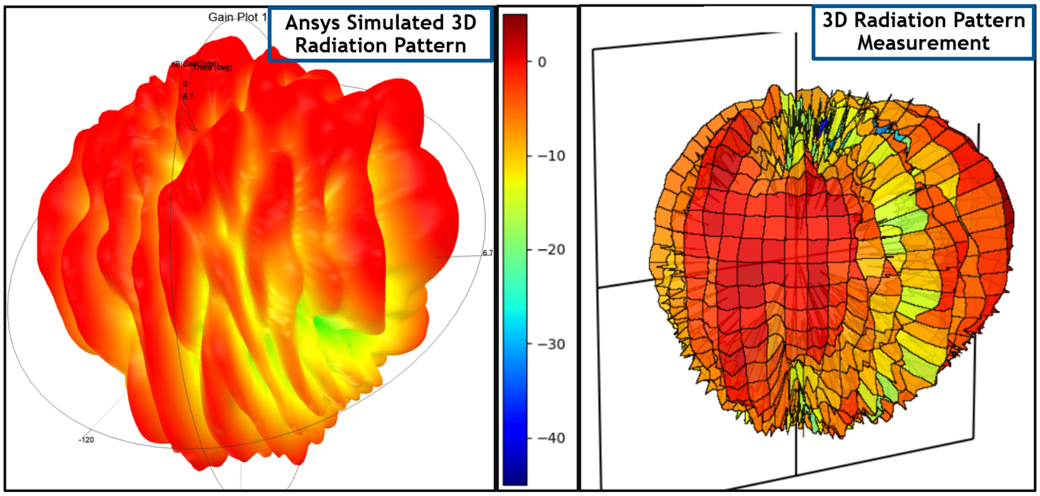

Figure 4.6: Simulated (left) and Measured (right) 3D radiation patterns.

4.3 High Impedance Surface novel Stacked Electromagnetic Band Gap (HIS-nSEBG)

In this section, we discuss the design of proposed novel EBG that we later embed in between the antennas to reduce SI in Section 4.4.

Among the various types of Electromagnetic Band Gap structures, the mushroom-like high-impedance surface EBG has become one of the most widely used designs [81]. While EBGs are relatively easy to design and fabricate, particularly for antenna applications, numerous innovative EBG designs have emerged in the literature, tailored for antenna applications in RF and microwave frequencies. As a result, EBGs have traditionally been employed in various antenna applications, such as enhancing antenna efficiency. For example, consider a microstrip patch antenna on a substrate material as depicted in Fig. 4.8 (top). Without the use of EBGs, a small percentage of the electric field power radiates from the patch antenna

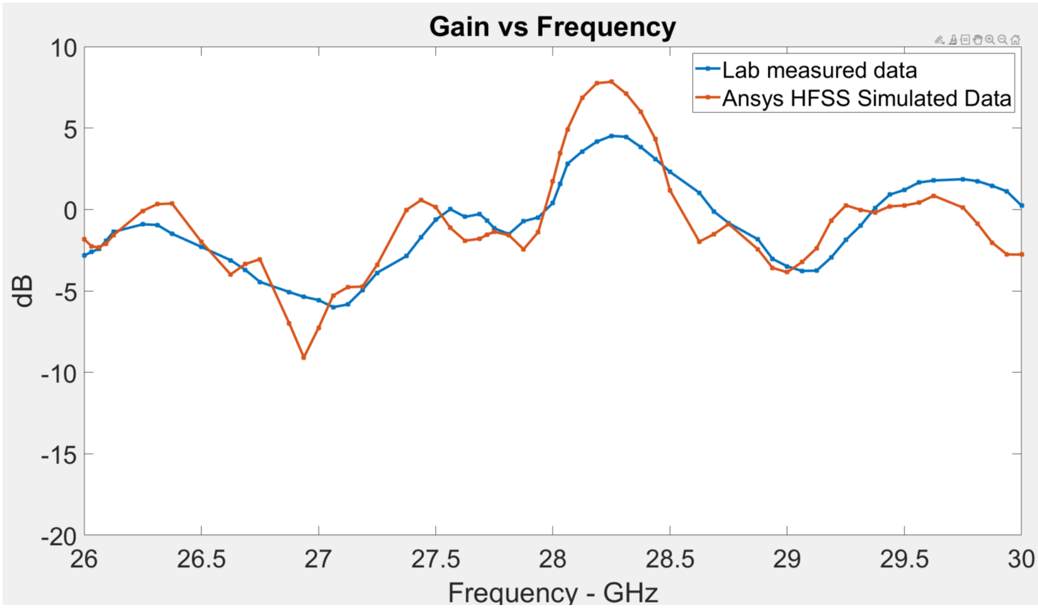

Figure 4.7: Frequency vs gain simulated (red) and measured (blue) plots showing measured peak gain of 4 dBi between 28 GHz and 28.5 GHz.

to free space and the remaining power leaks through the dielectric substrate [82] and copper layers as surface current waves. EBG can be used as part of the antenna design (Fig. 4.8 (bottom)) to suppress the surface waves and radiate more towards the main beam to increase the antenna efficiency.

In the proposed novel EBG, we develop a VicCross-like 2-layer stacked EBG structure to reduce the port-to-port coupling between the Tx and Rx antennas as a means for passive SI suppression in a mmWave FD radio design. Fig. 4.9 depicts a 2-stacked EBG structure in a 4-layer (top layer, second layer, third layer, and bottom layer) stack-up design. Stacked type EBG provides higher SI suppression and higher bandwidth compared to single stack mushroom EBG [49], [81], [83].

The surface impedance equation in Eq. (4.4) [84] guided our initial optimization

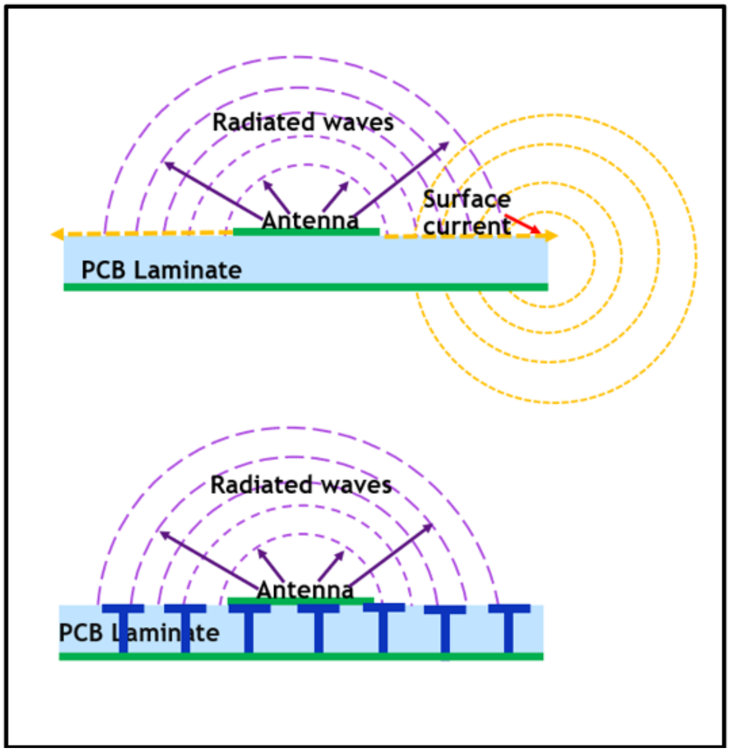

Figure 4.8: Top: Multi-path interference due to patch antenna destructive interference of surface current waves and antenna radiated waves resulting from using solid GND plane as reference GND for patch antenna design. Bottom: Mushroom EBG structures, as alternative to the solid ground plane, mitigate surface current propagation and radiation.

in determining the size of the through-hole via (which impacts inductance L) and the EBG shape (which impacts capacitance C):

$$Z_{surface} = \frac{j\omega L}{(1-\omega^2 LC)} \tag{4.4}$$

where ω is the angular frequency defined as ω = $2\pi f$, and f is the desired (resonant) frequency. Further, L and C can be modeled through the following equations:

$$L = \frac{\eta_s}{\omega} \times \tan(\beta h) \tag{4.5}$$

$$C = \frac{w\varepsilon_0(\varepsilon_{r1} + \varepsilon_{r2})}{\pi} \times \cosh^{-1}(\frac{D}{g}) \tag{4.6}$$

where $\eta_s = \sqrt{\mu_0\mu_r/\varepsilon_0\varepsilon_r}$ and $\beta_s = \omega\sqrt{\mu_0\mu_r\varepsilon_0\varepsilon_r}$ defined respectively as the intrinsic wave impedance and propagation constant. ε_0 and μ_0 denote the free space permittivity and permeability, respectively, and ε_r and μ_r are denote the corresponding relative values.

D, g and h are EBG pitch (EBG to EBG center), gap (EBG to EBG patch spacing) and EBG height, respectively

To create a high impedance surface, the denominator in Eq. (4.4) should be set to zero, which results in the following relationship between L, C, and f:

$$f_{resonance} = \frac{1}{2\pi \times \sqrt{LC}} \tag{4.7}$$

The overall operation of the via and EBG shape is modeled as an LC (resonant) circuit and at frequencies below the resonant frequency, the circuit model becomes inductive and supports TM (transverse magnetic) surface waves, whereas at frequencies above the resonant frequency, the circuit model becomes capacitive and thereby supports TE (transverse electromagnetic) surface waves. At a narrow band around the resonant frequency, surface impedance becomes very high [84].

The novel EBG shape and its stacked formation was implemented to further reduce the capacitance effect of the EBG patch (which was needed to increase the isolation bandwidth) and to limit further reduction in patch size to accommodate manufacturing limitations. Similar reduction in EBG patch capacitance through creating a novel EBG patch was carried out in [50] and described in Chapter 3 and is coined VicCross EBG. In comparison, [50] has a defected ground structure in addition to the VicCross EBG with different stackup and PCB material construction, while our new proposed HIS-nSEBG comprises of defected stacked patch EBGs with similar orientation for both top and inner layer EBG patches. Both designs have similar periodicity due to similar reduction on EBG patch capacitance that allows us to further improve isolation.

The final dimensions of the stacked EBG are shown in Fig. 4.9 and were achieved after extensive optimization using HFSS tool to provide a balance between antenna gain, isolation bandwidth, and port-to-port isolation. We refer to this EBG design as High Impedance Surface novel Stacked EBG.

Note that the patches on top and second layer of HIS-nSEBG need to be in the same orientation to allow for maximum coupling reduction of surface current waves. This is because with same patch orientation, the capacitance effect of the stacked patched are maximized and thereby reduce the effective coupling, which increases the isolation bandwidth.

4.4 EBG Integration with Antennas and Its Operation

In this section, we discuss the integration of the proposed HIS-nSEBG with the Tx and Rx antennas for a complete EBG-based FD antenna. We also discuss the operational aspects of the electric field coupling between the Tx and Rx antennas

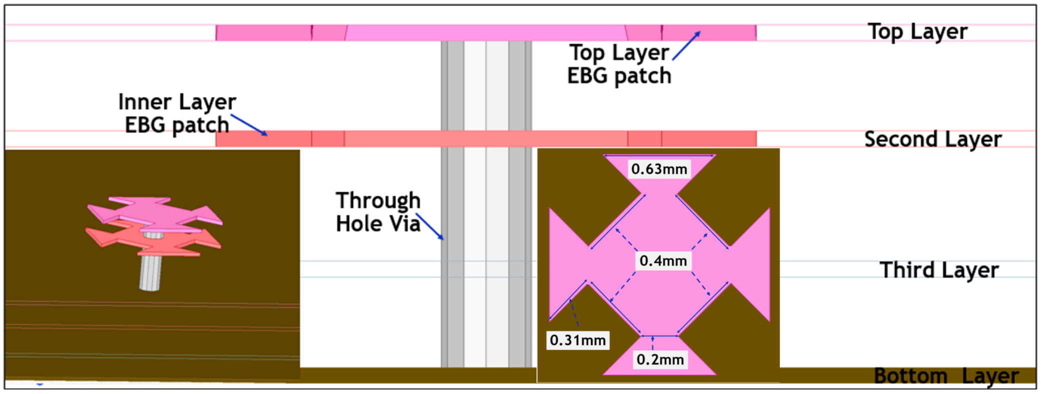

Figure 4.9: High Impedance Surface novel Stacked EBG 3D model structure in a 4-layer stack-up showing top and second layer patch with plated through hole via. The diameter of the through hole via is 0.2 mm. Substrate thickness is 850μm and the PCB material is RO435B Rogers laminate. The dimensions were finalized after numerous HFSS simulations to provide a balance between antenna gain, isolation bandwidth, and port-to-port cancellation.

resulting from the surface wave radiation through the substrate with and without the novel stacked EBG designs.

4.4.1 HIS-nSEBG Integration with Tx and Rx Antennas

The placement of HIS-nSEBG is optimized using Ansys HFSS simulations to achieve high SI suppression between the Tx and Rx antennas and also to achieve optimum Tx/Rx antenna gains by reducing unwanted surface wave radiation such as side lobes and back lobes.

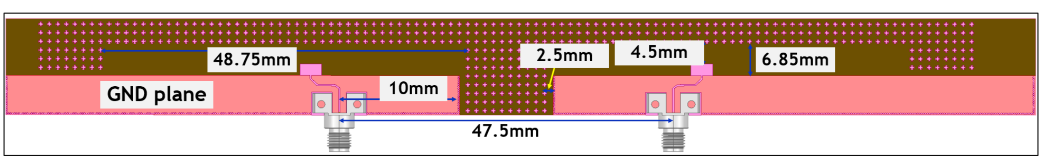

Figure 4.10: Transmit and Receive antenna elements relative to HIS-nSEBG.(picture not drawn to scale)

Fig. 4.10 shows the placement of HIS-nSEBG structures in between the Tx and Rx antennas. There are 10 columns of HIS-nSEBG structures placed at the center of the design between the Tx and Rx antennas, and the leftmost or rightmost EBG column is 2.5 mm from the solid GND plane. Further, there is 12.5 (10 + 2.5) mm distance between the Tx/Rx antenna transmission line and the leftmost/rightmost EBG column. There is a “guard ring" consisting of 3 rows of HIS-nSEBG along the top and 3x8 column of HIS-nSEBG at the left and right edge. This guard ring is shown in Fig. 4.10 and was optimized to provide optimum antenna gain and reduction in side lobe level and back side radiation level resulting from surface current propagation from transmit to receive antenna. Based on simulations, more than 4 mm minimum spacing is required between HIS-nSEBG and the antenna to achieve a reasonable gain and antenna efficiency.

Fig. 4.11 shows a close-up view of HIS-nSEBG integration with Tx and Rx antennas. HIS-nSEBG dimensions are shown in bottom left with top and second layer patches having the same width dimension of 1.2 mm with similar cutout dimensions of 0.3 mm, 0.4 mm, and 0.28 mm, respectively. Shielding vias, seen on bottom right, are placed at 0.25 mm distance from edge of the PCB to shield unwanted higher order electric and magnetic mode resonances, and to attenuate reflected surface current waves from the HIS-nSEBG.

The antenna to antenna pitch distance of 47.5 mm (almost 5λ) was optimized to allow for sufficient distance from center EBGs (to achieve high antenna gains) and to maximize the constructive interference between Tx and Rx antenna surface waves when the radio operates in the FD mode. Further, during the optimization of

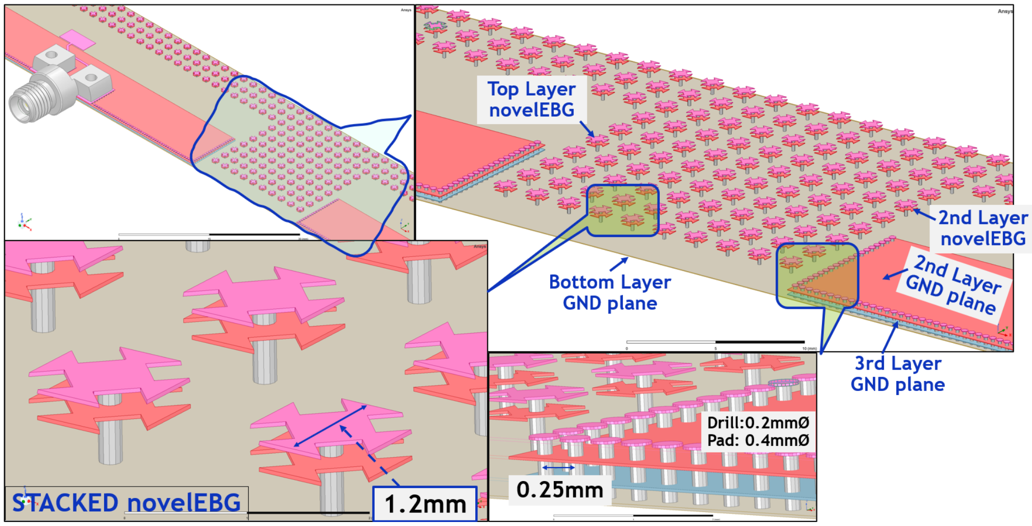

Figure 4.11: Top Left: HIS-nSEBG implementation in between Tx and Rx antennas. Top Right: Zoomed-in HIS-nSEBG showing top and second layer EBG patches. Bottom Left: HIS-nSEBG dimension of patches. Bottom Right: PCB stitching vias around EBG walls.

the HIS-nSEBG using HFSS, it is observed that the novel EBG supports TM surface waves at lower frequencies, TE surface waves at higher frequencies and both TM and TE in between the low and higher frequencies. However, at the resonance frequency, the imaginary part of the surface impedance of the HIS-nSEBG structure becomes large, where both TE and TM surface waves are suppressed, resulting in an electromagnetic surface wave bandgap thereby isolating the transmit and receive ports.

4.4.2 Operating Mechanism of HIS-nSEBG

The operating mechanism of SI suppression using the HIS-nSEBG described in this work is as seen in Fig. 4.12 based on HFSS simulation plots. From Fig. 4.12

top figure, the observed electric field excitation resulting from the movement of charges in the substrate and copper layers of PCB structure by the transmitting antenna is described by $\vec{E}$.

Through the direct coupling path, an electric field $\alpha\vec{E}$ is induced on the receiving antenna where α is modeled as the coupling coefficient. On the other hand, by adding HIS-nSEBG structures, a new path condition is generated for the electric field propagation. The coupling coefficient of the transmitting antenna to HIS-nSEBG is modeled by β_1 and the coupling coefficient between the HIS-nSEBG and the receiving antenna is modeled by β_2.

The total induced electric field force at the receiving antenna can be modeled as $(\alpha' + \beta_1\beta_2)\vec{E}$ and with properly designed passive SI suppression EBG structures in a transceiver system, the electric field in the scattering path is expected to produce a reverse coupling coefficient of the transmitted energy.

4.5 Measured and Simulation Results

In this section, we present the performance evaluation results of the overall antenna design with HIS-nSEBG embedded between the transmitting and receiving antennas. We use both HFSS simulations and over-the-air measurements of a fabricated prototype to derive these results.

4.5.1 Measurement Setup

The lab setup for the measurement of the FD antenna system is shown in Fig. 4.13. Anritsu 2-port VNA and RF cable assembly were used to connect to the antenna

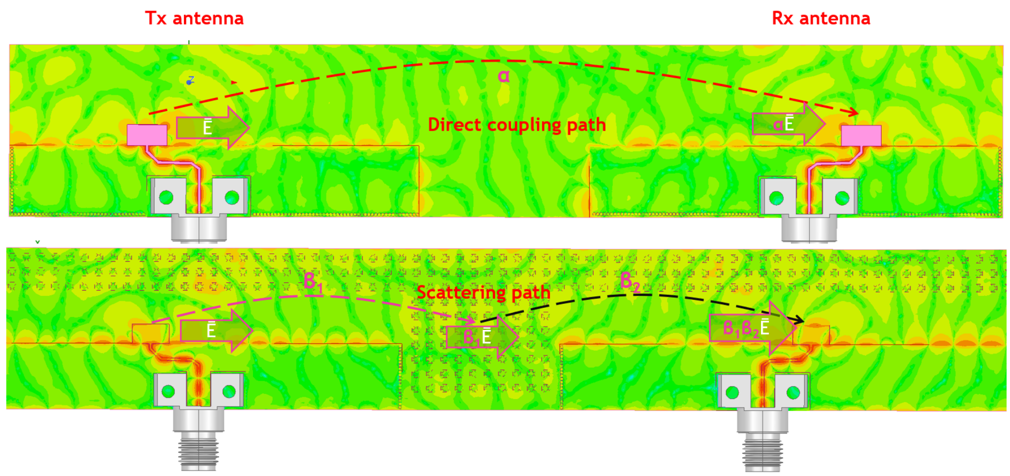

Figure 4.12: HIS-nSEBG (bottom figure) creates a scattering path within the EBG structure, which reduces the coupling between the antennas. The top figure shows the coupling between Tx and Rx ports/antennas without an EBG.

RF connector ports using a 2.4 mm to 2.92 mm adapter, similar to AUT setup in Section 4.3. This setup is used to measure the port-to-port isolation properties, in the form of scattering parameters, of the antenna system with HIS-nSEBG as well as a similar antenna setup that does not use any EBGs.

Scattering parameter measurement for the individual antenna elements within the FD system was also performed to make sure the performance matches measurements carried out in Section 4.1.

4.5.2 Self-Interference Suppression Performance

Fig. 4.14 shows the port-to-port isolation (i.e., SI reduction) results of the two antenna systems as a function of frequency (from 26 GHz to 30 GHz): one with HIS-nSEBG and one with no EBG. For each measured result, we also plot the

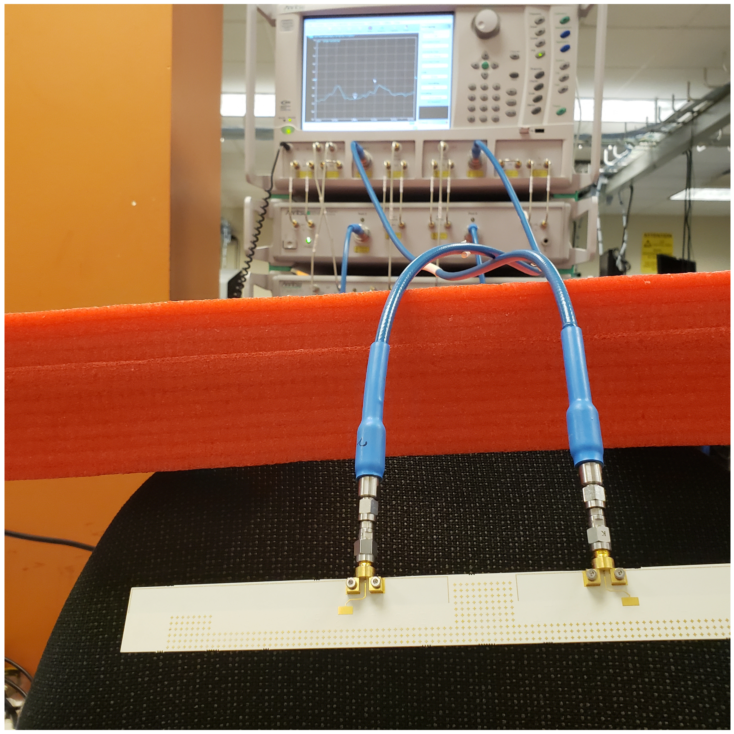

Figure 4.13: 2-Port Anritsu VNA lab measurement setup for gathering the return loss and isolation parameters for the antennas. The picture shows the fabricated antenna with integrated HIS-nSEBG.

predicted simulated results from HFSS.

It is observed that measured SI reduction is about -30 dB with no EBG, which is due to the over-the-air path loss. The introduction of HIS-nSBG provides an average of 25 dB additional reduction in SI over a 1 GHz bandwidth (27.5 GHz - 28.5 GHz). Also observed is that measured data (both with and without EBG) tracks the simulated data with only a few dB of difference, which shows high fidelity of the simulations in terms of characterizing reduction in SI.

Fig. 4.15 depicts a snapshot in time of the electromagnetic field distribution between the transmit and receiver antennas both with (bottom) and without (top)

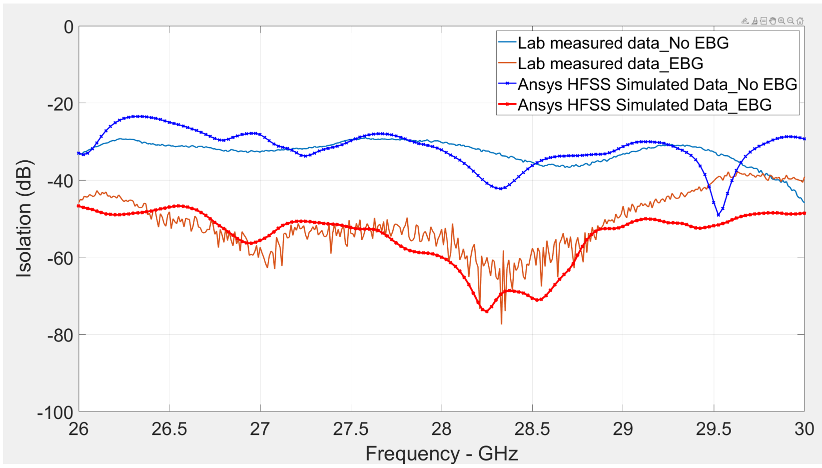

Figure 4.14: Simulated and measured SI suppression plots with and without HIS-nSEBG structures. Simulated and Measured data compared well across all frequency plots with only a few dB difference. Tx-Rx coupling without HIS-nSEBG (due to over-the-air path loss) is about -30 dB. HIS-nSEBG provides an average of 25 dB additional SI reduction around 27.5 GHz and 28.5 GHz frequency range of interest.

HIS-nSEBG. In the top figure, the TE mode of excited propagating electric field at 28 GHz traveling from Tx to Rx interferes with the propagating wave from Rx to Tx. Further, there is no structure in between the two antennas to create a high impedance path for the propagating fields.

On the other hand, the TE modes of excited propagated electric field with integrated HIS-nSEBG have less interference with one another, which is due to HIS-nSEBG's creation of the high impedance path.

Based on these results, we have successfully designed a derivative of the VicCross EBG, called the HIS-nSEBG, which was integrated with unit antenna elements. Its isolation characteristics were explored through both simulation and measurement data at the 28 GHz mmWave frequency. Furthermore, while most

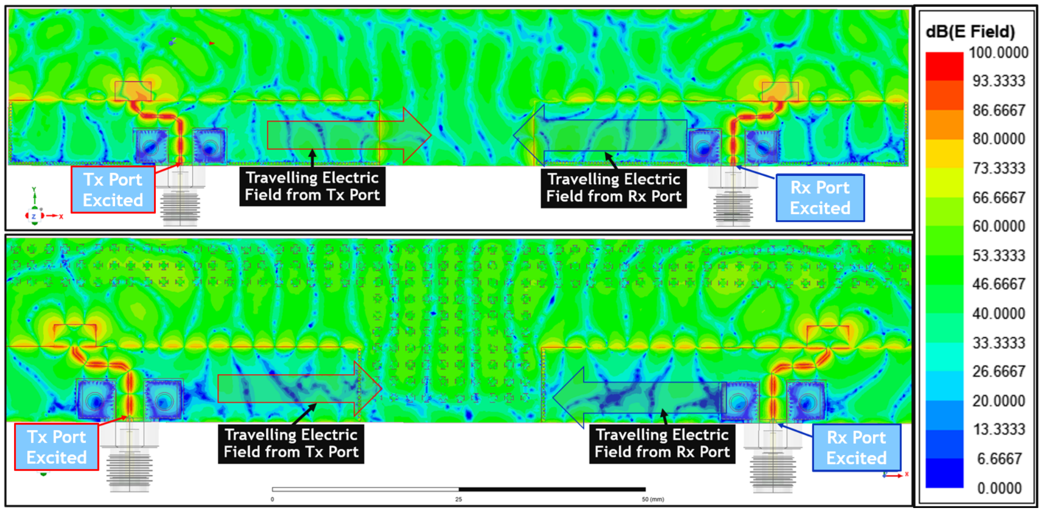

Figure 4.15: A snapshot of the electric field distribution when the radio operates in FD mode with HIS-nSEBG (bottom) and without EBG (top).

related work has focused on FD wireless in the context of sub-6 GHz radios, this study investigates mmWave FD radio design, specifically demonstrating the design and implementation of a novel EBG architecture. This architecture provides over 25 dB reduction in SI and marginally improves antenna performance in terms of gain and side-lobe levels. As discussed in Chapter 5, we extend this design to support multiple transmit and receive antennas and explore the joint operation of beamforming and antenna design to achieve further reductions in SI.

Chapter 5

HIS-nSEBG Isolation Improvement of MIMO Antenna

As a key technology for 5G, multiple-input and multiple-output (MIMO) uses multiple transmit (Tx) and receive (Rx) antennas to leverage multipath propagation, effectively increasing the capacity of a radio link [85]. Integrating FD with MIMO can enhance spectral efficiency, but both techniques require minimizing coupling between antenna elements, which becomes a major challenge for antenna designers, especially as the number of Tx/Rx chains increases as the radio node would contain N simultaneously active transceivers creating cross-interference between transmitter and receiver pairs from different transceivers. Physical separation of the transmit and receive antennas is an effective way to reduce the amount of interference between the Tx and Rx paths but requires more physical space and twice the number of antennas. Different methods to improve isolation in MIMO antenna configuration have been researched and few of the different techniques used are coupled line resonator [86], which employs a techniques that uses a a pair of parallel coupled-line resonators (PCRs) for isolation enhancement in planar microstrip patch array antennas. The proposed PCR-based decoupling unit cell provides additional 12 dB – 26.2 dB coupling reduction with an enhancement of antenna gain up to 1.25 dB. Neutralization line [87], [88] which consist of a dual-antenna, consisting of two symmetric antenna elements and three neutralization lines (NLs). The working mechanism of the three NLs is analyzed based on the S-parameters and surface current distributions. Polarization isolator [89] described a novel approach to suppress mutual coupling between patch antennas. A parasitic isolator, which is printed between the two patches, controls the polarization of the coupling field to reduce the antenna coupling. Measured results showed that this technique achieved isolation enhancement and cross-polarization level of 19.6 dB and 13.2 dB respectively. Capacitively-loaded loop (CLL) [90], described the capability of a magneto-dielectric superstrate to suppress the surface wave propagation. The capacitively loaded loop (CLL) meta-material (MTM) superstrate exhibits a high degree of surface wave attenuation and it is used to reduce the mutual coupling between the microstrip patch elements in MIMO antenna configurations. Meta-material superstrate [91] [92], described novel decoupling techniques for closely packed patch antennas using near filed resonators (NFR) and meta-surface superstrate structure to reduce mutual coupling. Split ring resonator (SRR) [93] [94], used one-dimensional electromagnetic band gap (1-D EBG) and split ring resonator (SRR) structures inserted between monopole antennas to suppress mutual coupling. The 1-D EBG and SRR function as a reflector and wave trap and are able to reduce mutual coupling between the antennas elements by more than 42 dB. The mushroom EBG described in [95] [96] use different configuration and designs to reduce planar surface wave between MIMO antenna elements. A new defected ground structure (DGS) in [97] is used to reduce the mutual coupling by controlling the polarization of the coupling field in addition to using two hybrid EBG structures with the ability to support and stop surface wave propagation are utilized simultaneously for achieving an extremely low envelope correlation coefficient (ECC). Also, [98] described a novel fractal DGS (FDGS) to reduce mutual coupling between coplanar spaced microstrip antenna elements. And lastly, meta-material absorber [99] employs the use of meta-material absorber (MA) to achieve high isolation between two patch antennas in a 2-element MIMO system operating at 5.5 GHz resonant frequency useful for WiMAX application.

The next chapter describes isolation improvement of MIMO antenna using novel HIS-nSEBG at mmWave frequency in a Transmit and Receive FD system environment.

5.1 HIS-nSEBG Extension to MIMO

In this section, we describe MIMO antenna array configuration using a 1x4 antenna array configuration without taking into account the effect of cross interference between Tx or Rx antenna elements. This chapter serves as an extension of Chapter 4 and leverages the unit antenna element design to configure MIMO antenna array. The novel HIS-nSEBG is then characterized in the MIMO environment and mutual coupling isolation is evaluated and data presented. Due to the type of VNA [79] used for the measurement of the prototyped 1x4 antenna array design, which consist of a 2-port network, individual transmit and receive antenna from the antenna array elements were considered at the same time in the mutual coupling isolation measurement. In line with our base assumption in Chapter 3 (Section 3.2), the inner edge and closest transmit and receive antenna will have lowest isolation while the farthest receive antenna would have higher isolation relative to the same inner edge transmit antenna. In addition, A single transmit antenna (inner edge antenna) was used as a transmitting element for all the individual receiver array antenna array during the FD isolation measurement. A comparison plot describing the different isolation measurement plots of individual unit antenna from Tx array to all unit antenna in Rx array is also discussed.

5.2 MIMO Antenna Configuration

This section details the antenna array measurement setup. The same Anritsu VNA, which was used for HIS-nSEBG characterization with a single antenna element for both Tx and Rx in Chapter 3, is utilized here. The VNA consists of a 2-port network terminal, which can be connected to our prototype MIMO antenna array element two ports at a time. This means that the VNA port can be connected to one Tx antenna element and one Rx antenna element at a time to characterize the HIS-nSEBG. Due to this limitation, we do not account for cross interference between the antenna elements within the array, either on the receiving or transmitting antenna. Additionally, the inner-edge transmitter antenna (Tx0) was used as the transmit antenna, while the receive antenna element alternated between Rx0, Rx1, Rx2, and Rx3. This arrangement is illustrated in Fig. 5.1

5.2.1 MIMO Antenna without EBG

To assess the impact of our HIS-nSEBG design, we measured the MIMO antenna array without the EBG, as shown in Fig. 5.1. The prototype antenna represents the Tx0 and Rx0 measurement setup for the edge antenna element of a MIMO antenna array.

Figure 5.1: 2-Port Anritsu VNA lab measurement setup for gathering port-to-port isolation parameters for MIMO antennas. The picture depicts Tx0 port and Rx0 port measurement.

The prototype MIMO antenna array is labeled from inside outwards with the edge Tx and Rx antenna element as Tx0 and Rx0 while the outermost antenna element is Tx3 and Rx3 respectively. Not included in the picture are the RF connectors for other Tx and Rx antenna elements. This was done to capture the mutual coupling effect of the edge Tx and Rx antenna elements, with and without populating the RF connectors to other antenna elements. Data suggest that the presence (with ideal 50 Ohm termination) and absence of RF connectors do not impact the isolation measurement of individual antenna element from Tx to Rx.

In subsequent measurements, we would populate the RF connectors for easy mating and de-mating to and from the VNA cable.

Subsequent measurements were performed using the same configuration depicted in Fig. 5.1, with the transmit antenna positioned at the array edge. In this setup, the second, third, and fourth receiver antennas were activated sequentially to characterize the mutual coupling between Tx0 and Rx1, Tx0 and Rx2, and Tx0 and Rx3. The mutual coupling data obtained from these measurements are analyzed and benchmarked against a comparable antenna prototype configuration incorporating an integrated HIS-nSEBG structure, with the comparative results detailed in Section 5.3.

5.2.2 MIMO Antenna with HIS-nSEBG

Fig.5.2 shows a MIMO antenna configuration involving elements Tx0 and Rx0, with a novel EBG structure fully integrated across the antenna array, including the inter-element region between the transmit and receive arrays. The coaxial input of the antenna is interfaced with a high-performance RF cable rated for up to 40 GHz bandwidth, which is connected to a VNA for S-parameter measurements.

The HIS-nSEBG structure implemented between adjacent antenna elements is

Figure 5.2: 2-Port Anritsu VNA lab measurement setup for gathering port-to-port isolation parameters for MIMO antennas with integrated HIS-nSEBG. The picture depicts Tx0 port and Rx0.

specifically designed to suppress near-field surface wave propagation and mitigate electromagnetic coupling from the transmit to the receive antennas. In FD operation, the receiver must operate concurrently and co-channel with the transmitter, leading to significant SI due to the high transmit power, often several orders of magnitude greater than the receiver's sensitivity threshold. By introducing the HIS-nSEBG, surface current coupling is effectively attenuated, thereby enhancing isolation and reducing SI at the receive ports.

To capture the SI or mutual coupling effect of the transmit antenna from other neighboring receiver antennas, measurements were carried out similar to section 5.2.1 to represent measurement setup for Tx0 and Rx1, Tx0 and Rx2, Tx0 and Rx3, respectively.

5.3 Measured Results

The measured results from the configurations detailed in Sections 5.2.1 and 5.2.2 are presented in Fig.5.3. The plot spans a 2 GHz frequency range and illustrates the isolation performance both with and without the HIS-nSEBG structure. In the figure, the solid continuous lines represent the MIMO antenna configuration with the full HIS-nSEBG implementation, while the dashed lines correspond to the configuration without the EBG.

The data show a consistent 20 dB improvement in isolation when comparing the configuration with HIS-nSEBG to that without it. Moreover, the isolation between Tx0 and the corresponding receiver antenna elements (Rx0, Rx1, Rx2, and Rx3) increases by approximately 5 dB for each successive receiver. These results are in line with theoretical expectations, confirming that both the increased physical separation between transmit and receive elements, as well as the integration of the HIS-nSEBG, contribute to enhanced isolation in the MIMO antenna system. In the higher frequency range of 28.4 GHz to 29 GHz, it is observed that the isolation with the HIS-nSEBG remains invariant regardless of the separation distance between Tx0 and Rx1 through Rx3. This behavior is also evident in the isolation results for the configuration without HIS-nSEBG within the same frequency band. The causes of this phenomenon are currently under investigation; however, it is hypothesized that it may be attributed to the constructive mode alignment of the surface wave propagation which could lead to a phase synchronization effect that diminishes the impact of varying element separation.

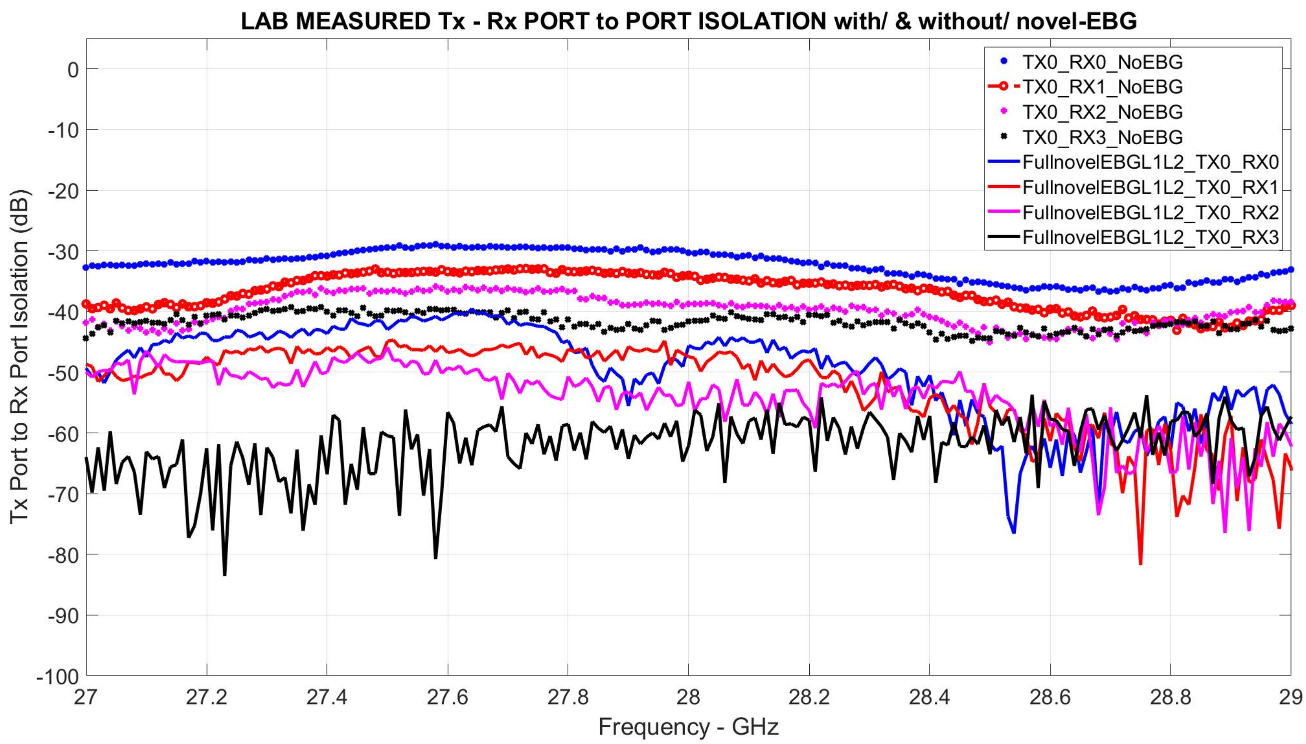

Figure 5.3: Port-to-Port Isolation for MIMO antenna with and without HIS-nSEBG. Blue plot lines showed Tx0 and Rx0 isolation, Red plot lines showed Tx0 and Rx1 isolation, Pink plot lines showed Tx0 and Rx2 isolation, Black plot lines showed Tx0 and Rx3 isolation respectively.

The measurements reported here do not include the additional transmit antenna elements—Tx1, Tx2, and Tx3—and their corresponding receiver elements in the Rx array. It is hypothesized that the isolation results for these additional transmit antenna elements would demonstrate further improvements. This is based on the expected reduction in mutual coupling due to their relative spatial separation from the receiver elements. Specifically, Tx1 and Rx0 would exhibit higher isolation compared to Tx0 and Rx0, Tx1 and Rx1 would show greater isolation than Tx0 and Rx1, and so on. Similarly, Tx2 and Tx3 would experience less coupling with Rx0 compared to Tx0 and Tx1 with Rx0, and similarly for other receiver elements.

In conclusion, the integration of the HIS-nSEBG structure within the MIMO antenna array has been shown to significantly improve isolation between transmit and receive antenna elements, particularly within the measured frequency range. The results confirm the theoretical expectations that increasing spatial separation between antenna elements, coupled with the HIS-nSEBG, enhances mutual isolation. Additionally, the hypothesis that isolation performance improves with the relative positioning of transmit and receive elements, especially for antenna elements further separated in the array, is supported by the observed data. While the measurements presented focus on Tx0 and its corresponding Rx elements, it is anticipated that similar improvements will be observed for the other transmit elements (Tx1, Tx2, Tx3), with further reduction in mutual coupling due to their increased separation. The findings highlight the efficacy of the HIS-nSEBG in mitigating self-interference and enhancing the overall performance of full-duplex MIMO antenna systems.

Chapter 6

Conclusion

In this dissertation, we considered the problem of passive self-interference cancellation in mmWave FD systems.

Specifically, we developed a novel EBG structure, named VicCross EBG, along with a resonant GND slot, through extensive simulations using HFSS Tool. This VicCross EBG design was integrated between the transmit and receive MIMO array antennas operating in a FD environment. The VicCross EBG is intended to create a high impedance path that minimizes electromagnetic wave propagation between the transmitting and receiving MIMO array antennas. The innovation of this EBG lies in the reduction of capacitance of the mushroom EBG patch and its design for operation at 28 GHz to achieve wideband isolation. The high impedance characteristics were validated through a signal scattering matrix and plotted using HFSS tool. In the FD system, the VicCross EBG demonstrated through simulation an improved isolation between the transmitter and receiver antennas of up to 70 dB or higher at 28 GHz, with a bandwidth exceeding 100 MHz.

To enable the manufacturability of our novel EBG and enable active characterization in a practical FD system, we further optimized the VicCross EBG through extensive simulations and developed a stacked version of the design, referred to as High Impedance Surface novel Stacked EBG. Initial characterization of this stacked EBG involved the use of a unit transmit and receive antenna. We performed passive measurement of the unit antenna and compared the results with simulated data to ensure that simulations accurately predict performance of antenna element. The performance evaluation, which included isolation measurement characterization and simulations of the novel EBG integrated with the unit antenna elements in FD system, showed good agreement within 2-dB of deviation across the frequency bandwidth of measurement. The results indicated approximately 30 dB isolation between the transmitter and receiver, in comparison to a system without the EBG.

We expanded our simulation, manufacturing, and measurement of the HIS-nSEBG design to include MIMO antenna arrays. The HIS-nSEBG was integrated between a 1x4 MIMO antenna array, and its performance was evaluated through measurements. We employed a 2-port VNA to assess the the impact of the novel EBG in isolating the transmitter array from the receiver array antennas. In the MIMO setup, the isolation achieved was approximately 20 dB when compared to a full-duplex system without the EBG.

Our results show that a combination of antenna separation and EBG integration can reduce SI by more than 70 dB. Thus, the results presented in this dissertation show that we can build mmWave FD radios by primarily canceling SI through passive antenna design along with active beamforming and digital cancellation. This can potentially eliminate the need for complex and bulky analog cancellation techniques, paving the way to build compact and low cost mmWave FD radios.

Chapter 7

Major Dissertation Contributions

7.1 Major Contributions

The primary contribution of this dissertation is the development and comprehensive characterization of a passive SIC methodology for FD communication systems, targeting both infrastructure nodes and UE operating at mmWave frequencies. The research focuses on the design, electromagnetic modeling, full-wave simulation, and experimental verification of novel EBG structures. These EBGs are strategically integrated between co-located transmit and receive antenna elements to suppress near-field coupling and mitigate self-interference within compact FD antenna architectures. The following sections provide a detailed exposition of these contributions.

- A novel EBG structure was developed, incorporating analytical modeling and full-wave electromagnetic simulation, aimed at achieving passive self-interference suppression in the mmWave frequency spectrum..
- The proposed EBG structure features a highly compact footprint, facilitating its integration into space-limited mmWave front-end architectures, such as those in 5G and future 6G systems. Despite its reduced size, the design

meets the stringent isolation and self-interference suppression requirements essential for FD operation.

- The proposed FD antenna designs contribute to the advancement of mmWave wireless systems by effectively passively mitigating self-interference, thereby obviating the need for intricate and bulky analog SIC techniques. This enables the possibility of performing complete residual interference cancellation within the digital domain, enhancing system efficiency and simplifying the overall architecture.

Finally, a custom mmWave measurement test bench was developed, employing National Instruments (NI) and TMYTEK mmWave transceiver modules and components, to facilitate the experimental Over-the-air (OTA) characterization of passive self-interference isolation in FD antenna systems. Initial tests were conducted using an off-the-shelf antenna array, and over-the-air (OTA) data was collected by measuring throughput and signal-to-noise ratio (SNR) at the receiver. However, due to equipment malfunction, we were unable to complete the final testing of the prototyped HIS-nSEBG design, as detailed in the following chapter. Nevertheless, we successfully established a mmWave full-duplex (FD) test bench, which will be used to characterize the HIS-nSEBG prototype in an FD environment.

Chapter 8

Research Limitations and Future Work

In this section, we outline several key research challenges that, if addressed, could have improved the efficiency of data acquisition in this study. Additionally, we explore the opportunities and potential avenues for future work in the context of mmWave FD wireless communication.

8.1 Limitations

Listed below are some of the ways that this research can be expanded and improved.

8.1.1 Multiple Port VNA

In the characterization of port-to-port isolation for the MIMO array configuration discussed in Chapter 5, a 2-port VNA was utilized to measure the isolation between individual transmit and receive antenna elements, capturing their respective isolation performance in isolation from one another. It would have been easier to use a higher port VNA. The integration of multi-port VNAs, such as the Keysight M9485A PXI VNA [100] or Transcom's T-Series multi-port VNAs [101], facilitates simultaneous multi-port measurements, thereby enhancing the efficiency and accuracy of characterizing complex antenna systems.The T58XX series VNAs are capable of performing parallel testing on designs under test (DUTs) with up to 10 ports or conducting simultaneous measurements across multiple DUTs. Similarly, the Keysight M9485A PXI VNA offers a versatile and scalable platform, addressing the increasing complexity of high-performance measurement tasks. By leveraging either of these VNAs, comprehensive MIMO antenna array measurements for FD systems can be conducted. This configuration facilitates concurrent transmission from multiple transmit ports and simultaneous reception on multiple receive ports, enabling advanced isolation and interference characterization critical for mmWave FD applications.

8.1.2 Active Measurement Test Bench

An active measurement test bench was established to assess the FD functionality of the radio architecture. This setup includes key FD radio components: the National Instruments Software Defined Radio (USRP2943R), TMYTEK Up-Down (UD) Converter, Beamformer, along with coaxial and Ethernet cabling, enabling comprehensive evaluation of the FD radio system's performance and interference characteristics.

A physical test bench, as shown in Fig. 8.1, was established utilizing an off-the-shelf 4x4 antenna array for OTA signal transmission and reception between the USRP devices. The beamformer, integrated with the antenna array, was positioned 1.5 feet apart to facilitate proper signal exchange. Additionally, a custom software graphical user interface (GUI) was configured for controlling each device in the

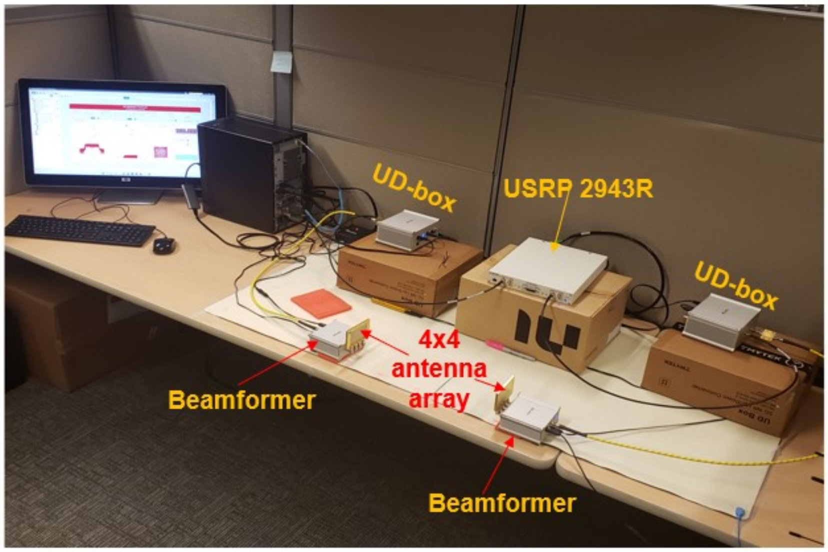

Figure 8.1: Active measurement Test bench set up showing National Instrument Software Defined Radio (USRP2943R), TMYTEK Up-Down Converter and Beamformer.

setup.

The purpose of the test bench, depicted in Fig. 8.1, is twofold: first, to perform OTA measurements using the standard 4x4 antenna array, and second, to replace this array with a prototyped 1x4 MIMO full-duplex (FD) antenna array. This configuration enables validation of the test bench by ensuring successful data/packet transmission between the base station (USRP) and UE (USRP), and allows for the investigation of beam steering effects at the transmitter on mmWave signal reception at the receiver.

During the test measurement phase, the transmitter UD-Box sustained damage due to electrostatic discharge (ESD), which compromised its functionality. The faulty device has been sent to the manufacturer for repair or replacement. As of the time of writing this dissertation, the device had not yet been returned, thereby preventing the completion of the intended active measurements with our prototyped antenna array. The absence of the UD-Box precluded the execution of the active measurement tests, which were designed to assess signal transmission and reception within a FD operational environment.

8.1.3 MIMO Array OTA Measurement

OTA measurements were not conducted with the 1x4 MIMO antenna array due to its 4-port configuration. The mmWave anechoic chamber, which was used for OTA characterization of single-port antenna elements, does not have the infrastructure to accommodate and measure a 4-port antenna array. The 1x4 MIMO array was specifically designed to integrate directly into the active measurement setup, as shown in Fig. 8.1. The TMYTEK beamformer, equipped with a 4-port terminal, supports the connection of four input antenna elements to form the array. It utilizes internal phase shifters to manage beamforming and control the radiated power distribution across the antenna array.

8.2 Future Work

In this section, we discuss some ideas to expand the work proposed in this thesis.

8.2.1 Active Measurement Characterization

The active measurement setup, as illustrated in Fig.8.1, will be employed alongside the prototyped antenna array. Two TMYTEK UD-Box devices will be positioned in parallel to establish a full-duplex node, enabling measurement operations as shown in Fig.8.2. This configuration allows for a comprehensive joint characterization of beamforming techniques and antenna design with respect to their influence on FD wireless system performance. In typical mmWave systems, analog beamforming is optimized to maximize beamforming gain in a targeted direction. However, a trade-off exists where some of this gain may be deliberately sacrificed at both the transmit and receive ends to reduce SI. The integrated design of such beamforming strategies, in conjunction with the proposed antennas, aligns with active SI cancellation approaches and offers a compelling area for future research advancements.

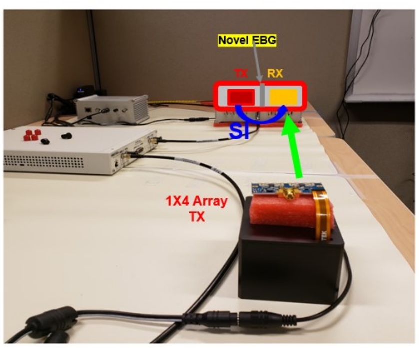

mmWave bench set-up

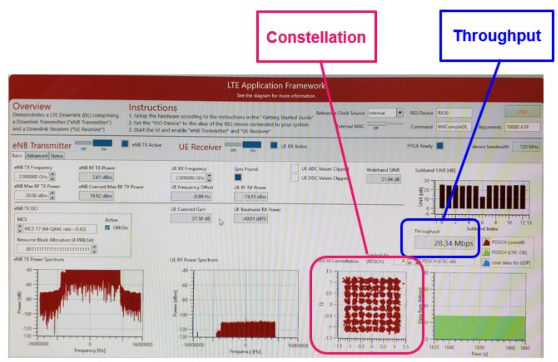

SDR GUI showing Receiver 64QAM constellation and SNR

Figure 8.2: Active measurement Test bench set up showing National Instrument Software Defined Radio (USRP2943R), TMYTEK Transceiver device with integrated 1x4 modular antenna array facing TMYTEK Beam Former device with a cartoon of prototype MIMO antenna array with integrated HIS-nSEBG.

Active measurement data can be collected using the LTE application framework on the test devices, as demonstrated in Fig. 8.2, right image. The primary metrics for evaluating isolation between the Tx and Rx antennas include the I-Q constellation diagram, receiver throughput, and signal-to-noise ratio (SNR). These parameters are essential for quantifying the performance of the full-duplex system and assessing the effectiveness of self-interference mitigation techniques.

Bibliography

[1] F. Guo, F. R. Yu, H. Zhang, X. Li, H. Ji, and V. C. M. Leung, "Enabling Massive IoT Toward 6G: A Comprehensive Survey," *IEEE Internet of Things Journal*, vol. 8, no. 15, pp. 11 891–11 915, 2021. DOI: 10.1109/JIOT.2021.3063686.

[2] G. Lan, Z. Liu, Y. Zhang, T. Scargill, J. Stojkovic, C. Joe-Wong, and M. Gorlatova, "Edge-assisted Collaborative Image Recognition for Mobile Augmented Reality," *ACM Transactions on Sensor Networks*, vol. 18, no. 1, pp. 1–31, 2021. DOI: 10.1145/3469033.

[3] T. Kim, J. Zuo, X. Zhang, and C. Joe-Wong, "Edge-msl: Split learning on the mobile edge via multi-armed bandits," in *IEEE INFOCOM 2024 - IEEE Conference on Computer Communications*, 2024, pp. 391–400. DOI: 10.1109/INFOCOM52122.2024.10621231.

[4] A. Sabharwal, P. Schniter, D. Guo, D. W. Bliss, S. Rangarajan, and R. Wichman, "In-Band Full-Duplex Wireless: Challenges and Opportunities," *IEEE Journal on Selected Areas in Communications*, vol. 32, no. 9, pp. 1637–1652, 2014. DOI: 10.1109/JSAC.2014.2330193.

[5] J. I. Choi, M. Jain, K. Srinivasan, P. Levis, and S. Katti, "Achieving Single Channel, Full Duplex Wireless Communication," in *16th Annual International Conference on Mobile Computing and Networking (MOBICOM)*, Sep. 2010.

[6] M. Duarte and A. Sabharwal, "Full-duplex wireless communications using off-the-shelf radios: Feasibility and first results," in *2010 Conference Record of the Forty Fourth Asilomar Conference on Signals, Systems and Computers*, 2010, pp. 1558–1562. DOI: 10.1109/ACSSC.2010.5757799.

[7] E. Aryafar, M. A. K. K. Sundaresan, S. Rangarajan, and M. Chiang, "MIDU: Enabling MIMO Full Duplex," in *18th Annual International Conference on Mobile Computing and Networking (MOBICOM)*, Aug. 2012.

[8] B. Smida, A. Sabharwal, G. Fodor, G. C. Alexandropoulos, H. A. Suraweera, and C.-B. Chae, "Full-Duplex Wireless for 6G: Progress Brings New Opportunities and Challenges," *IEEE Journal on Selected Areas in Communications*, vol. 41, no. 9, pp. 2729–2750, Sep. 2023, ISSN: 0733-8716, 1558-0008. DOI: 10.1109/JSAC.2023.3287612. [Online]. Available: https://ieeexplore.ieee.org/document/10158724/ (visited on 02/24/2024).

[9] M. L. Roy, P. Bantavis, A. Pérennec, R. Lababidi, and D. L. Jeune, "Multilayer miniaturized wideband electromagnetic band-gaps for wideband full-duplex transceiver," in *2018 48th European Microwave Conference (EuMC)*, 2018, pp. 636–639. DOI: 10.23919/EuMC.2018.8541402.

[10] J. R. Krier and I. F. Akyildiz, "Active self-interference cancellation of passband signals using gradient descent," in *2013 IEEE 24th Annual International Symposium on Personal, Indoor, and Mobile Radio Communications (PIMRC)*, 2013, pp. 1212–1216. DOI: 10.1109/PIMRC.2013.6666323.

[11] H. Luo, M. Holm, and T. Ratnarajah, "On the performance of active analog self-interference cancellation techniques for beyond 5g systems," *China Communications*, vol. 18, no. 10, pp. 158–168, 2021. DOI: 10.23919/JCC.2021.10.011.

[12] N. Reiskarimian, M. B. Dastjerdi, J. Zhou, and H. Krishnaswamy, "Analysis and design of commutation-based circulator-receivers for integrated full-duplex wireless," *IEEE Journal of Solid-State Circuits*, vol. 53, no. 8, pp. 2190–2201, 2018. DOI: 10.1109/JSSC.2018.2828827.

[13] A. Alshammari, A. Iqbal, R. B. Simorangkir, S. Hongjian, and I. B. Mabrouk., "Ultra-miniaturized in-band full-duplex implantable antenna for wireless capsule endoscopy," in *2024 IEEE International Symposium on Antennas and Propagation and INC/USNC-URSI Radio Science Meeting (AP-S/INC-USNC-URSI)*, 2024, pp. 2401–2402. DOI: 10.1109/AP-S/INC-USNC-URSI52054.2024.10685918.

[14] A. Sikder, A. Kumar, G. Srivastava, and A. Mohan, "Linearly co-polarized dual band in-band full-duplex antenna system with defected ground structure," in *2024 Second International Conference on Microwave, Antenna and Communication (MAC)*, 2024, pp. 1–5. DOI: 10.1109/MAC61551.2024.10837073.

[15] L. Ma, C. Gu, and J. Mao, "A compact high isolation co-linearly polarized microstrip patch antenna for full-duplex integrated sensing and communication," in *2024 IEEE 12th Asia-Pacific Conference on Antennas and Propagation (APCAP)*, 2024, pp. 1–2. DOI: 10.1109/APCAP62011.2024.10881832.

[16] F. Yang and Y. Rahmat-Samii, "Microstrip antennas integrated with electromagnetic band-gap (ebg) structures: A low mutual coupling design for array applications," *IEEE Transactions on Antennas and Propagation*, vol. 51, no. 10, pp. 2936–2946, 2003. DOI: 10.1109/TAP.2003.817983.

[17] A. K. Oladeinde, E. Aryafar, and B. Pejcinovic, "Ebg-based self-interference cancellation to enable mmwave full-duplex wireless," in *2021 IEEE Texas Symposium on Wireless and Microwave Circuits and Systems (WMCS)*, 2021, pp. 1–6. DOI: 10.1109/WMCS52222.2021.9493285.

[18] A. K. Oladeinde, E. Aryafar, and B. Pejcinovic, "Mmwave tx-rx self-interference suppression through a high impedance surface stacked ebg," *Electronics*, vol. 13, no. 15, 2024, ISSN: 2079-9292. DOI: 10.3390/electronics13153067. [Online]. Available: https://www.mdpi.com/2079-9292/13/15/3067.

[19] S. Goyal, P. Liu, S. S. Panwar, R. A. Difazio, R. Yang, and E. Bala, "Full duplex cellular systems: Will doubling interference prevent doubling capacity?" *IEEE Communications Magazine*, vol. 53, no. 5, pp. 121–127, 2015. DOI: 10.1109/MCOM.2015.7105650.

[20] K. M. Thilina, H. Tabassum, E. Hossain, and D. I. Kim, "Medium access control design for full duplex wireless systems: Challenges and approaches," *IEEE Communications Magazine*, vol. 53, no. 5, pp. 112–120, 2015. DOI: 10.1109/MCOM.2015.7105649.

[21] T. Vial, A. Lefevre, M. Le Penven, and Q. Bodinier, "A short review of current challenges and potential applications of full duplex in wireless networks," in *2017 XXXIInd General Assembly and Scientific Symposium of the International Union of Radio Science (URSI GASS)*, 2017, pp. 1–4. DOI: 10.23919/URSIGASS.2017.8105051.

[22] L. Wang, F. Tian, T. Svensson, D. Feng, M. Song, and S. Li, "Exploiting full duplex for device-to-device communications in heterogeneous networks," *IEEE Communications Magazine*, vol. 53, no. 5, pp. 146–152, 2015. DOI: 10.1109/MCOM.2015.7105653.

[23] M. G. Sarret, G. Berardinelli, N. H. Mahmood, B. Soret, and P. Mogensen, "Can full duplex reduce the discovery time in d2d communication?" In *2016 International Symposium on Wireless Communication Systems (ISWCS)*, 2016, pp. 27–31. DOI: 10.1109/ISWCS.2016.7600849.

[24] *The potential of full duplex in beyond 5g and 6g*, https://www.free6gtraining.com/2022/02/the-potential-of-full-duplex-in-beyond.html, Feb. 2022.

[25] A. K. Khandani, "Methods for Spatial Multiplexing of Wireless Two-Way Channels," in *US Patent US7817641*, 2010.

[26] H. Yon, N. H. Abd Rahman, M. A. Aris, M. H. Jamaluddin, I. K. Chen Lin, H. Jumaat, F. N. M. Redzwan, and Y. Yamada, "Development of C-Shaped Parasitic MIMO Antennas for Mutual Coupling Reduction," in *Electronics 2021, 10(19), 2431; https://doi.org/10.3390/electronics10192431*, 2021.

[27] X -J. Lin, Z. -M. Xie, and P. -S. Zhang, "Integrated Filtering Microstrip Duplex Antenna Array with High Isolation," in *International Journal of Antennas Propagation. vol. 2017, Article ID 4127943, 8 pages, 2017. https://doi.org/10.1155/2017/4127943*, 2017.

[28] E. Aryafar and A. Keshavarz-Haddad, "Fd2: A directional full duplex communication system for indoor wireless networks," in *2015 IEEE Conference on Computer Communications (INFOCOM)*, 2015, pp. 1993–2001. DOI: 10.1109/INFOCOM.2015.7218583.

[29] H. Hosseini, A. Almutairi, S. M. Hashir, E. Aryafar, and J. Camp, "An outdoor experimental study of many antenna full-duplex wireless," in *2023 35th International Teletraffic Congress (ITC-35)*, 2023, pp. 1–5. DOI: 10.1109/ITC-3560063.2023.10555581.

[30] H. Hosseini, A. Almutairi, S. M. Hashir, E. Aryafar, and J. Camp, "An Experimental Study on Beamforming Architecture and Full-Duplex Wireless Across Two Operational Outdoor Massive MIMO Networks," in *Elsevier Performance Evaluation Journal*, 2024. DOI: 10.1016/j.peva.2024.102447.

[31] K. E. Kolodziej, J. G. McMichael, and B. T. Perry, "Multitap rf canceller for in-band full-duplex wireless communications," *IEEE Transactions on Wireless Communications*, vol. 15, no. 6, pp. 4321–4334, 2016. DOI: 10.1109/TWC.2016.2539169.

[32] N. Reiskarimian, M. B. Dastjerdi, J. Zhou, and H. Krishnaswamy, "Analysis and design of commutation-based circulator-receivers for integrated full-duplex wireless," *IEEE Journal of Solid-State Circuits*, vol. 53, no. 8, pp. 2190–2201, 2018. DOI: 10.1109/JSSC.2018.2828827.

[33] V. Singh, S. Mondal, A. Gadre, M. Srivastava, J. Paramesh, and S. Kumar, "Millimeter-Wave Full Duplex Radios," in *Proceedings of ACM MobiCom. Article No. 2, Pages 1–14, https://doi.org/10.1145/3372224.3380879*, April 2020.

[34] E. Everett, A. Sahai, and A. Sabharwal, "Passive self-interference suppression for full-duplex infrastructure nodes," *IEEE Transactions on Wireless Communications*, vol. 13, no. 2, pp. 680–694, 2014. DOI: 10.1109/TWC.2013.010214.130226.

[35] W. Slingsby and J. McGeehan, "Antenna isolation measurements for on-frequency radio repeaters," in *1995 Ninth International Conference on Antennas and Propagation, ICAP '95 (Conf. Publ. No. 407)*, vol. 1, 1995, 239–243 vol.1. DOI: 10.1049/cp:19950300.

[36] A. Ramos, T. Varum, and J. N. Matos, "A review on mutual coupling reduction techniques in mmwaves structures and massive mimo arrays," *IEEE Access*, vol. 11, pp. 143 143–143 166, 2023. DOI: 10.1109/ACCESS.2023.3343107.

[37] D. Wu, S. W. Cheung, Q. L. Li, and T. I. Yuk, "Decoupling using diamond-shaped patterned ground resonator for small mimo antennas," *IET Microwaves, Antennas & Propagation*, vol. 11, no. 2, pp. 177–183, 2017. DOI: https://doi.org/10.1049/iet-map.2016.0400.

[38] H. Nawaz and I. Tekin, "Dual-polarized, differential fed microstrip patch antennas with very high interport isolation for full-duplex communication," *IEEE Transactions on Antennas and Propagation*, vol. 65, no. 12, pp. 7355–7360, 2017. DOI: 10.1109/TAP.2017.2765829.

[39] C.-Y.-D. Sim, C.-C. Chang, and J.-S. Row, "Dual-feed dual-polarized patch antenna with low cross polarization and high isolation," *IEEE Transactions on Antennas and Propagation*, vol. 57, no. 10, pp. 3321–3324, 2009. DOI: 10.1109/TAP.2009.2028702.

[40] K. Iwamoto, M. Heino, K. Haneda, and H. Morikawa, "Design of an antenna decoupling structure for an inband full-duplex collinear dipole array," *IEEE Transactions on Antennas and Propagation*, vol. 66, no. 7, pp. 3763–3768, 2018. DOI: 10.1109/TAP.2018.2835301.

[41] A. Madni and W. T. Khan, "Design of a compact 4-element gnss antenna array with high isolation using a defected ground structure (dgs) and a microwave absorber," *IEEE Open Journal of Antennas and Propagation*, vol. 4, pp. 779–791, 2023. DOI: 10.1109/OJAP.2023.3298773.

[42] S. Ghosh, T.-N. Tran, and T. Le-Ngoc, "Dual-layer ebg-based miniaturized multi-element antenna for mimo systems," *IEEE Transactions on Antennas and Propagation*, vol. 62, no. 8, pp. 3985–3997, 2014. DOI: 10.1109/TAP.2014.2323410.

[43] H. S. Farahani, M. Veysi, M. Kamyab, and A. Tadjalli, "Mutual coupling reduction in patch antenna arrays using a uc-ebg superstrate," *IEEE Antennas and Wireless Propagation Letters*, vol. 9, pp. 57–59, 2010. DOI: 10.1109/LAWP.2010.2042565.

[44] M. J. Al-Hasan, T. A. Denidni, and A. R. Sebak, "Millimeter-wave compact ebg structure for mutual coupling reduction applications," *IEEE Transactions on Antennas and Propagation*, vol. 63, no. 2, pp. 823–828, 2015. DOI: 10.1109/TAP.2014.2381229.

[45] L. Qiu, F. Zhao, K. Xiao, S.-L. Chai, and J.-J. Mao, "Transmit–receive isolation improvement of antenna arrays by using ebg structures," *IEEE Antennas and Wireless Propagation Letters*, vol. 11, pp. 93–96, 2012. DOI: 10.1109/LAWP.2012.2183847.

[46] K. Wei, J.-Y. Li, L. Wang, Z.-J. Xing, and R. Xu, "Mutual coupling reduction by novel fractal defected ground structure bandgap filter," *IEEE Transactions on Antennas and Propagation*, vol. 64, no. 10, pp. 4328–4335, 2016. DOI: 10.1109/TAP.2016.2591058.

[47] J. Qiang, F. Xu, and W. Fan, "Reducing mutual coupling of millimeter wave array antennas by fractal defected ground structure," in *2018 12th International Symposium on Antennas, Propagation and EM Theory (ISAPE)*, 2018, pp. 1–3. DOI: 10.1109/ISAPE.2018.8634210.

[48] S. Dey, S. Dey, and S. K. Koul, "Isolation improvement of mimo antenna using novel ebg and hair-pin shaped dgs at 5g millimeter wave band," *IEEE Access*, vol. 9, pp. 162 820–162 834, 2021. DOI: 10.1109/ACCESS.2021.3133324.

[49] A. K. Oladeinde, S. Shippey, E. Aryafar, and B. Pejcinovic, "Ebg placement optimization in a via-fed stacked patch antenna for full-duplex wireless," in *2022 IEEE-APS Topical Conference on Antennas and Propagation in Wireless Communications (APWC)*, 2022, pp. 021–026. DOI: 10.1109/APWC49427.2022.9899980.

[50] A. K. Oladeinde, E. Aryafar, and B. Pejcinovic, "Ebg-based self-interference cancellation to enable mmwave full-duplex wireless," in *2021 IEEE Texas Symposium on Wireless and Microwave Circuits and Systems (WMCS)*, 2021, pp. 1–6. DOI: 10.1109/WMCS52222.2021.9493285.

[51] A. E. I. Lamminen, A. R. Vimpari, and J. Saily, "Uc-ebg on ltcc for 60-ghz frequency band antenna applications," *IEEE Transactions on Antennas and Propagation*, vol. 57, no. 10, pp. 2904–2912, 2009. DOI: 10.1109/TAP.2009.2029311.

[52] *3d electromagnetic field simulator for rf and wireless design*, https://www.ansys.com/products/electronics/ansys-hfss.

[53] IEEE 802.11 Standard, "IEEE 802.11ad, amendment 3: Enhancements for very high throughput in the 60 GHz band," 2012.

[54] 5G PPP, "The 5G infrastructure public private partnership," in *https://5g-ppp.eu/*.

[55] *5G Millimeter Wave Auction Winners: AT&T, T-Mobile, Verizon, Windstream, Starry, and Others*, https://www.telecompetitor.com/5g-millimeter-wave-auction-winners-att-t-mobile-verizon-windstream-starry-and-others/.

[56] *AT&T Enhances Spectrum Position Following FCC Auction 102*, https://about.att.com/story/2019/att_enhances_spectrum_position.html.

[57] *An evaluation of AT&T millimeter wave markets*, https://www.allnetinsights.com/blogs/news/at-t-millimeter-wave-markets.

[58] *Ericsson mobility report: on the pulse of the networked society*, https://www.gsma.com/latinamerica/ericsson-mobility-report-networked-society/.

[59] A. Sabharwal, P. Schniter, D. Guo, D. W. Bliss, S. Rangarajan, and R. Wichman, “In-band full-duplex wireless: Challenges and opportunities,” *IEEE Journal on Selected Areas in Communications*, vol. 32, no. 9, pp. 1637–1652, 2014. DOI: 10.1109/JSAC.2014.2330193.

[60] E. Aryafar and A. Keshavarz-Haddad, “Pafd: Phased array full-duplex,” in *IEEE INFOCOM 2018 - IEEE Conference on Computer Communications*, 2018, pp. 261–269. DOI: 10.1109/INFOCOM.2018.8486358.

[61] *Femto forum, "interference management in umts femtocels,"* Feb. 2010.

[62] M. A. Khojastepour, K. Sundaresan, S. Rangarajan, X. Zhang, and S. Barghi, “The case for antenna cancellation for scalable full-duplex wireless communications,” New York, NY, USA: Association for Computing Machinery, 2011, ISBN: 9781450310598. DOI: 10.1145/2070562.2070579. [Online]. Available: https://doi.org/10.1145/2070562.2070579.

[63] E. Everett, M. Duarte, C. Dick, and A. Sabharwal, “Empowering full-duplex wireless communication by exploiting directional diversity,” in *2011 Conference Record of the Forty Fifth Asilomar Conference on Signals, Systems and Computers (ASILOMAR)*, 2011, pp. 2002–2006. DOI: 10.1109/ACSSC.2011.6190376.

[64] E. Everett, A. Sahai, and A. Sabharwal, “Passive self-interference suppression for full-duplex infrastructure nodes,” *IEEE Transactions on Wireless Communications*, vol. 13, no. 2, pp. 680–694, 2014. DOI: 10.1109/TWC.2013.010214.130226.

[65] M. Duarte, C. Dick, and A. Sabharwal, “Experiment-driven characterization of full-duplex wireless systems,” *IEEE Transactions on Wireless Communications*, vol. 11, no. 12, pp. 4296–4307, 2012. DOI: 10.1109/TWC.2012.102612.111278.

[66] S. Chen, M. Beach, and J. McGeehan, “Division-free duplex for wireless applications,” English, *Electronics Letters*, vol. 34, no. 2, pp. 147–148, Jan. 1998, ISSN: 1350-911X. DOI: 10.1049/el:19980022.

[67] M. Duarte, A. Sabharwal, V. Aggarwal, R. Jana, K. K. Ramakrishnan, C. W. Rice, and N. K. Shankaranarayanan, "Design and characterization of a full-duplex multiantenna system for wifi networks," *IEEE Transactions on Vehicular Technology*, vol. 63, no. 3, pp. 1160–1177, 2014. DOI: 10.1109/TVT.2013.2284712.

[68] K. Lin, R. Messerian, and Y. Wang, "A digital leakage cancellation scheme for monostatic fmcw radar," in *2004 IEEE MTT-S International Microwave Symposium Digest (IEEE Cat. No.04CH37535)*, vol. 2, 2004, 747–750 Vol.2. DOI: 10.1109/MWSYM.2004.1339068.

[69] E. Antonio-Rodríguez, R. López-Valcarce, T. Riihonen, S. Werner, and R. Wichman, "Adaptive self-interference cancellation in wideband full-duplex decode-and-forward mimo relays," in *2013 IEEE 14th Workshop on Signal Processing Advances in Wireless Communications (SPAWC)*, 2013, pp. 370–374. DOI: 10.1109/SPAWC.2013.6612074.

[70] E. Antonio-Rodríguez, R. López-Valcarce, T. Riihonen, S. Werner, and R. Wichman, "Autocorrelation-based adaptation rule for feedback equalization in wideband full-duplex amplify-and-forward mimo relays," in *2013 IEEE International Conference on Acoustics, Speech and Signal Processing*, 2013, pp. 4968–4972. DOI: 10.1109/ICASSP.2013.6638606.

[71] J. Zhou, N. Reiskarimian, J. Diakonikolas, T. Dinc, T. Chen, G. Zussman, and H. Krishnaswamy, "Integrated full duplex radios," *IEEE Communications Magazine*, vol. 55, no. 4, pp. 142–151, 2017. DOI: 10.1109/MCOM.2017.1600583.

[72] *Ro3000 series circuit material: Ro3003, ro3006, ro3010 and ro3035 high frequency laminate*, Available at: https://www.rogerscorp.com.

[73] F. Yang and Y. Rahmat-Samii, *Electromagnetic band gap structures in antenna engineering*. New York, NY, USA: Cambridge University Press, 2008, ISBN: 052188991X.

[74] N. Kushwaha and R. Kumar, "Study of different shape electromagnetic band gap (ebg) structures for single and dual band application," in *Journal of Microwave, Optoelectronics and Electromagnetic Applications*, 2014.

[75] P. Deo, D. Mirshekar-Syahkal, and G. Zheng, "Ebg enhanced broadband dual antenna configuration for passive self-interference suppression in full-duplex communications," in *2018 15th European Radar Conference (EuRAD)*, 2018, pp. 461–464. DOI: 10.23919/EuRAD.2018.8546551.

[76] *Active-s parameter measurement and plot in hfss*, http://www.ece.uprm.edu/~rafaelr/inel6068/HFSS/hfss_onlinehelp.pdf.

[77] *Ansys HFSS*, https://www.ansys.com/products/electronics/ansys-hfss.

[78] F. Yang and Y. Rahmat-Samii, "Electromagnetic Band Gap Structures in Antenna Engineering," in *Cambridge University Press, New York, NY, USA*, 2008.

[79] *Anritsu Test and Measurement Equipment*, https://www.anritsu.com/en-us/.

[80] *MilliBox: Benchtop mmWave Antenna Test System*, https://millibox.org/.

[81] M. A. M. Hassan and A. A. Kishk, "Bandwidth study of the stacked mushroom ebg unit cells," *IEEE Transactions on Antennas and Propagation*, vol. 65, no. 8, pp. 4357–4362, 2017. DOI: 10.1109/TAP.2017.2710258.

[82] F. Yang and Y. Rahmat-Samii, "Reflection phase characterizations of the ebg ground plane for low profile wire antenna applications," *IEEE Transactions on Antennas and Propagation*, vol. 51, no. 10, pp. 2691–2703, 2003. DOI: 10.1109/TAP.2003.817559.

[83] T. Jiao, T. Jiang, and Y. Li, "Antenna array coupling reduction based on stacked ebg structures," in *2017 International Applied Computational Electromagnetics Society Symposium (ACES)*, 2017, pp. 1–2.

[84] D. M. Elsheakh, H. A. Elsadek, and E. A. Abdallah, "Antenna designs with electromagnetic band gap structures," in *Metamaterial*, X.-Y. Jiang, Ed., Rijeka: IntechOpen, 2012, ch. 16. DOI: 10.5772/37222. [Online]. Available: https://doi.org/10.5772/37222.

[85] J. G. Andrews, S. Buzzi, W. Choi, S. V. Hanly, A. Lozano, A. C. K. Soong, and J. C. Zhang, "What will 5g be?" *IEEE Journal on Selected Areas in Communications*, vol. 32, no. 6, pp. 1065–1082, 2014. DOI: 10.1109/JSAC.2014.2328098.

[86] K. S. Vishvaksenan, K. Mithra, R. Kalaiarasan, and K. S. Raj, "Mutual coupling reduction in microstrip patch antenna arrays using parallel coupled-line resonators," *IEEE Antennas and Wireless Propagation Letters*, vol. 16, pp. 2146–2149, 2017. DOI: 10.1109/LAWP.2017.2700521.

[87] Y. Wang and Z. Du, "A wideband printed dual-antenna with three neutralization lines for mobile terminals," *IEEE Transactions on Antennas and Propagation*, vol. 62, no. 3, pp. 1495–1500, 2014. DOI: 10.1109/TAP.2013.2295226.

[88] S. Zhang and G. F. Pedersen, "Mutual coupling reduction for uwb mimo antennas with a wideband neutralization line," *IEEE Antennas and Wireless Propagation Letters*, vol. 15, pp. 166–169, 2016. DOI: 10.1109/LAWP.2015.2435992.

[89] Y.-F. Cheng, X. Ding, W. Shao, and B.-Z. Wang, "Reduction of mutual coupling between patch antennas using a polarization-conversion isolator," *IEEE Antennas and Wireless Propagation Letters*, vol. 16, pp. 1257–1260, 2017. DOI: 10.1109/LAWP.2016.2631621.

[90] A. Jafargholi, A. Jafargholi, and J. H. Choi, "Mutual coupling reduction in an array of patch antennas using cll metamaterial superstrate for mimo applications," *IEEE Transactions on Antennas and Propagation*, vol. 67, no. 1, pp. 179–189, 2019. DOI: 10.1109/TAP.2018.2874747.

[91] Z. Wang, L. Zhao, Y. Cai, S. Zheng, and Y. Yin, "A meta-surface antenna array decoupling (maad) method for mutual coupling reduction in a mimo antenna system," *Scientific reports*, vol. 8, no. 1, p. 3152, 2018.

[92] M. Li, B. G. Zhong, and S. W. Cheung, "Isolation enhancement for mimo patch antennas using near-field resonators as coupling-mode transducers," *IEEE Transactions on Antennas and Propagation*, vol. 67, no. 2, pp. 755–764, 2019. DOI: 10.1109/TAP.2018.2880048.

[93] Z. Qamar, U. Naeem, S. A. Khan, M. Chongcheawchamnan, and M. F. Shafique, "Mutual coupling reduction for high-performance densely packed patch antenna arrays on finite substrate," *IEEE Transactions on Antennas and Propagation*, vol. 64, no. 5, pp. 1653–1660, 2016. DOI: 10.1109/TAP.2016.2535540.

[94] J.-Y. Lee, S.-H. Kim, and J.-H. Jang, "Reduction of mutual coupling in planar multiple antenna by using 1-d ebg and srr structures," *IEEE Transactions on Antennas and Propagation*, vol. 63, no. 9, pp. 4194–4198, 2015. DOI: 10.1109/TAP.2015.2447052.

[95] F. Yang and Y. Rahmat-Samii, "Microstrip antennas integrated with electromagnetic band-gap (ebg) structures: A low mutual coupling design for array applications," *IEEE Transactions on Antennas and Propagation*, vol. 51, no. 10, pp. 2936–2946, 2003. DOI: 10.1109/TAP.2003.817983.

[96] Y. Liu, X. Yang, Y. Jia, and Y. J. Guo, "A low correlation and mutual coupling mimo antenna," *IEEE Access*, vol. 7, pp. 127 384–127 392, 2019. DOI: 10.1109/ACCESS.2019.2939270.

[97] S. Hwangbo, H. Y. Yang, and Y.-K. Yoon, "Mutual coupling reduction using micromachined complementary meander-line slots for a patch array antenna," *IEEE Antennas and Wireless Propagation Letters*, vol. 16, pp. 1667–1670, 2017. DOI: 10.1109/LAWP.2017.2663114.

[98] K. Wei, J.-Y. Li, L. Wang, Z.-J. Xing, and R. Xu, "Mutual coupling reduction by novel fractal defected ground structure bandgap filter," *IEEE Transactions on Antennas and Propagation*, vol. 64, no. 10, pp. 4328–4335, 2016. DOI: 10.1109/TAP.2016.2591058.

[99] P. Garg and P. Jain, "Isolation improvement of mimo antenna using a novel flower shaped metamaterial absorber at 5.5 ghz wimax band," *IEEE Transactions on Circuits and Systems II: Express Briefs*, vol. 67, no. 4, pp. 675–679, 2020. DOI: 10.1109/TCSII.2019.2925148.

[100] https://www.keysight.com/us/en/product/M9485A/pxie-multiport-vector-network-analyzer.html.

[101] https://awt-global.com/wp3/vector-network-analyzers/vector-network-analyzers-multi-port/.